

**CLOUD COVERAGE DURING FIRE ACE  
DERIVED FROM AVHRR DATA**

Patrick Minnis  
Atmospheric Sciences  
NASA Langley Research Center  
Hampton, VA 23681

David R. Doelling, Venkatesan Chakrapani, Douglas A. Spangenberg,  
Louis Nguyen, Rabindra Palikonda  
AS & M Inc.  
Hampton, VA 23666

Taneil Uttal  
NOAA/ ETL  
Boulder, CO

Robert F. Arduini  
SAIC  
Hampton, VA 23666

Matthew Shupe  
Science and Technology Corporation  
Boulder, CO

November 1999  
Submitted to *FIRE ACE Special Issue, Journal of Geophysical Research*

## Abstract

Cloud cover and height are derived from NOAA-12 and 14 Advanced Very High Resolution Radiometer (AVHRR) over the Arctic Ocean for an  $8^{\circ}$  latitude by  $30^{\circ}$  longitude domain centered on the Surface Heat Budget of the Arctic Ocean ship *Des Groseilliers*. Multispectral thresholds were determined subjectively and applied to each image providing excellent temporal coverage during the May-July 1998 First ISCCP Regional Experiment Arctic Clouds Experiment (FIRE ACE). Mean cloud amounts were near 70% for the entire period but varied regionally from 55 to 85%. These values are typical for this part of the Arctic suggesting that FIRE ACE was conducted in representative conditions. A diurnal cycle of mean cloud amount was found for the domain during June and July having a range of 10% with a mid-to-late morning maximum. The AVHRR-derived cloud amounts are in excellent agreement with visual and radar measurements taken from the *Des Groseilliers*, except for a few subvisual and low cloud cases. Average AVHRR-derived cloudiness differ by  $-1$  to  $+3\%$  from the mean values derived from the surface compared to 5-25% underestimates from previous satellite retrievals. The satellite-derived cloud heights are very accurate for low clouds. Higher cloud altitudes are less certain because cloud optical depths were not available to adjust the temperature observed for the optically thin high clouds and the radiating temperature of many of the high clouds was representative of some altitude deep in the cloud rather than the cloud top. The development of a more accurate automated method for detecting polar clouds at AVHRR wavelengths will require inclusion of variable thresholds to account for the angular dependence of the surface reflectance and the seasonally changing albedos of the ice pack. Use of a  $1.6\text{-}\mu\text{m}$  channel on the AVHRR or other instrument complement will greatly enhance the capabilities for detecting clouds over poles during summer.

## 1. INTRODUCTION

Clouds are an important part of the Arctic climate because of their effects on the radiation budget and their role in the hydrological cycle. The First ISCCP (International Satellite Cloud Climatology Project) Regional Experiment (FIRE) Arctic Clouds Experiment [ACE; *Curry et al.*, 1999] was undertaken to obtain a better characterization of Arctic clouds and their interactions with the surface, radiation fluxes, and the atmosphere. The combination of instruments on the Surface Heat Budget of the Arctic Ocean (SHEBA) ship *Des Groseilliers* [*Perovich et al.*, 1999], aircraft, and satellites furnished the measurements needed to accomplish this goal. The ship was frozen in the ice for a year and moved with the pack. The surface and aircraft data give the details necessary to study specific micro- or cloud-scale processes, while the satellites provide the large-scale context and spatial information. Because of its remoteness, satellites are the most effective means for monitoring clouds over the Arctic Ocean. The surface and aircraft measurements can also serve to validate and ensure reliability of the satellite retrievals.

To obtain a useful accounting of clouds in the Arctic, it is first necessary to accurately detect clouds in the imagery. Typically, satellite-observed visible (VIS;  $0.65\ \mu\text{m}$ ) and infrared (IR;  $11\ \mu\text{m}$ ) radiance data are used to derive cloud fraction, temperature, and optical depth. However, the extremely bright and variable VIS surface albedos and diminished thermal IR contrast between low clouds and the surface make the detection of clouds from satellite data a difficult process in polar regions. Atmospheric conditions in the Arctic do not often meet the satellite retrieval assumptions that clouds are colder and brighter than the surface. A variety of approaches has been developed to overcome the difficulties imposed by the polar surface on satellite detection of clouds. Only a few are noted here because many of these methods have already been discussed by *Curry et al.* [1996].

The most promising techniques use solar-infrared (SI;  $3.7\ \mu\text{m}$ ) or multispectral infrared and/or microwave data, in addition to the conventional VIS and IR data. Solar infrared is used to denote radiation in the  $3.5 - 4.0\ \mu\text{m}$  region because there can be significant contributions to the total radiance from both solar reflection and terrestrial and cloud emission. *Key and Barry* [1989] used sets of fixed VIS, SI, and IR thresholds to improve the detection of clouds over polar ice and snow. The SI reflectance of the large snow grains is typically very small so that the brightness temperature difference (BTD) between the SI and IR temperatures is also relatively small during the daytime. The initial ISCCP algorithm has recently been enhanced to use a solar-zenith-angle dependent SI threshold in addition to the usual VIS and IR thresholds to detect clouds over snow near the poles [*Rossow et al.*, 1996]. Although the use of the SI data has improved the detection capabilities over the poles [*Rossow et al.*, 1999], the latest ISCCP approach still underestimates cloud fraction by 10 - 50% relative to surface observations during the Arctic summer [*Schweiger et al.*, 1999]. The Improved Initialization Inversion (3I) algorithm [*Chedin et al.*, 1985] used to analyze the High Resolution Infrared Radiation Sounder (HIRS) and Microwave Sounding Unit (MSU) data yields greater cloud fractions that vary between 0

and 18% less than the corresponding surface observations during Arctic summer [Schweiger *et al.*, 1999]. One of the greatest difficulties in formulating methods for polar cloud detection is ground truth. The availability of the unique SHEBA surface-based cloud fraction and altitude dataset taken during FIRE ACE makes it possible to evaluate satellite-based cloud detection over the Arctic in more detail than heretofore possible.

In this paper, a less objective approach is taken to derive cloud amount, temperature, and height from Advanced Very High Resolution Radiometer (AVHRR) VIS, SI, and IR data during the FIRE ACE period over a meso-to-large-scale domain centered on the *Des Groseilliers* to provide an accurate quantification of these fields. These cloud properties are used to relate the FIRE ACE period to the Arctic climatology and to understand the uncertainties in commonly used detection methods. Additionally, the careful examination and comparison of the subjectively derived thresholds to theoretical calculations can be used to guide the development of improved automated detection methods over snow and ice. The results of this study will be valuable for studying meso-scale cloud processes during FIRE ACE, cloud radiative effects [Doelling *et al.*, 1999], and large-scale cloud microphysical properties.

## 2. DATA

### a. AVHRR

NOAA-12 (N12) and NOAA-14 (N14) AVHRR High-Resolution Picture Transmission (HRPT) 1-km images were collected during FIRE-ACE covering the period from April 1 through August 15, 1998 (see <http://www-pm.larc.nasa.gov/sat.gif> for imagery). The images were initially centered near the *Des Groseilliers* position and consisted of 600 lines by 1300 elements to include the domain between 72°N to 80°N and 180°W to 150°W (figure 1). The center point of the retrieved images varied as the ship moved until July 1 when the center point was fixed because the limited range of the satellite receiving station restricted the spatial coverage. As seen in figure 2, these two satellites provide good diurnal sampling except between 1800 and 2400 local time (LT). Only data taken during the FIRE ACE period between 3 May and 31 July 1998 are analyzed here. The images for each overpass do not always provide complete coverage of the domain, so there is incomplete sampling over the domain.

A variation of the *Nguyen et al.* [1999] technique was used to normalize the calibration of each N12 channel to its N14 counterpart. The N12 counts for the visible (0.65- $\mu$ m) and near-infrared (0.87  $\mu$ m) channels were regressed against the corresponding N14 counts during each month of the FIRE-ACE period using collocated data taken over the Arctic. Data were used in the normalization regressions only if they were taken within 10 min of each other and with a viewing zenith  $\theta$  differences no greater than 1°. Because of the relative azimuth  $\psi$  angle varied rapidly with scan position, only data taken within 17° of nadir were used in the correlations.

A scatterplot of the coincident channel-1 VIS and channel-2 near-infrared (NIR; 0.87  $\mu$ m) data and the regression fits are shown in figure 3 for May. The normalization equation is

$$C_{N14} = a_o + a_l C_{N12}, \quad (1)$$

where the 10-bit N12 and N14 counts are  $C_{N12}$  and  $C_{N14}$ , respectively. The coefficients did not vary significantly between each month between April and July, so mean coefficients were used for the entire period. For the VIS channel  $a_o = -1.8$  and  $a_l = 1.035$ ,  $a_o = 0.4$  and  $a_l = 1.038$  for the NIR channel. These coefficients result in normalized N12 counts that are within  $\pm 0.4\%$  of the counts predicted using a different fit for each month.

The N14 or normalized N12 VIS and NIR counts are converted to narrowband radiances  $L_v$  using the *Rao and Chen* [1996 and update] degradation equations for N14. The narrowband VIS albedo is

$$\alpha_v = L_v / [D(d) \mu_o E \chi(\mu_o, \mu, \psi)] \quad (2)$$

where  $D$  is the Earth-Sun distance correction factor for Julian day  $d$ ,  $E$  is the visible solar constant for N14 ( $511 \text{ Wm}^{-2}\text{sr}^{-1}\mu\text{m}^{-1}$ ), and  $\mu$  and  $\mu_o$  are the cosines of the satellite viewing and solar zenith  $\theta_o$  angles. The narrowband bidirectional anisotropic reflectance factors  $\chi$  from *Minnis and Harrison* [1984] were used for clear ocean and cloudy scenes, while the Earth Radiation Budget Experiment broadband bidirectional model [*Suttles et al.*, 1998] is used for clear snow or ice scenes. The channel-2 albedos were computed in a similar fashion.

The onboard calibration of the three thermal infrared channels of AVHRR should eliminate the need to normalize the N12 with N14 temperatures. However, these channels were also examined to ensure consistency. The equivalent blackbody temperatures  $T$  are related with the regression equation,

$$T_{N14} = b_o + b_l T_{N12}, \quad (3)$$

where the subscripts N12 and N14 refer to N12 and N14, respectively. The mean values for the coefficients  $b_o$  and  $b_l$  are 5.10 and 0.983 for channel 4 (IR;  $10.8 \mu\text{m}$ ) and 4.60 and 0.985 for channel 5 ( $12.0 \mu\text{m}$ ), respectively. The bias between N14 and N12 for both channels is less than 0.5K suggesting that there may be a slight difference in the onboard blackbody source. This possibility is consistent with the channel-3 (SI;  $3.75 \mu\text{m}$ ) temperature differences. The mean difference between the N14 and N12 channel-3 temperatures for  $T_3 > 245 \text{ K}$  is 0.8 K. The subscript 3 refers to channel 3. Because of the solar-reflected component in channel 3, colder temperatures were not observed over the domain during this sunlit period for the matched N12 and N14 overpasses. A comparison of N12 and N14 channel-3 and channel-4 data taken during night over other areas during this time period reveals some striping in the  $T_3$  temperature range observed during FIRE ACE. The standard deviation in the nighttime difference between  $T_3$  and  $T_4$  increases with decreasing temperature and corresponds to the striping evident in the channel-3 imagery (e.g., *Warren*, 1989). At 240K, the standard deviations are 2.0 and 1.3K for N12 and

N14, respectively, and appear to decrease to less than 1 K at 250K. This striping will affect cloud detection at very cold temperatures. The inter-satellite biases in the thermal channel calibrations were not included in the analysis because they are so small.

*b. Surface data*

Temperature and humidity profiles nominally taken close to 0000, 0600, 1200, and 1800 UTC with rawinsondes launched from the *Des Groseilliers* were used to characterize the vertical atmospheric structure. These soundings were interpolated to the time of each overpass and are assumed to be representative of the entire domain. Cloud amount in octas was determined every 3 hours through visual observation from the ship. The NOAA Environmental Technology Laboratory Program millimeter cloud radar (MMCR) on the ship was also used to determine cloud fraction directly overhead by counting the number of beams with returns over  $-50$  dBz in any gate over a 30-min period centered on each overpass. A return was considered significant if its intensity exceeded  $-50$  dBz. Cloud boundaries were determined using a combination of the MMCR, Atmospheric Radiation Measurement (ARM) Belfort ceilometer, and 523-nm Depolarization and Backscatter-Unattended Lidar data using the technique of *Clothiaux et al.* [1999].

### 3. SCENE IDENTIFICATION

Each image was manually examined to select a set of thresholds. The VIS, SI, and IR channel and BTM images were inspected for obviously clear regions within the domain using an interactive data analysis system. The maximum mean BTM values corresponding to the clear areas were computed for each image to obtain the BTM thresholds. All threshold determinations for the images were completed independently of and prior to receipt of the surface visual and radar observations. Each pixel was classified as clear ocean, snow, or cloudy using the following parameters: the VIS reflectance;  $T_4$ , the channel-4 temperature;  $\Delta T_{34}$ , the difference of  $T_3$  and  $T_4$ ; and  $\Delta T_{45}$ , the difference of  $T_4$  and  $T_5$ , the channel-5 temperature (12- $\mu$ m). The selections were made as follows. If

$$\alpha_v < 0.08 \delta(\theta_o) \text{ and } T_4 > 270\text{K},$$

then the pixel is clear ocean. The normalized directional reflectance model  $\delta$  from Minnis and Harrison (1984) is used to model the normalized clear ocean albedo as a function of  $\theta_o$ . A pixel is classified as cloudy if any of the following tests are satisfied.

$$\Delta T_{34} > \Delta T_{34}(\text{CLD}), \tag{4a}$$

or 
$$\Delta T_{45} > \Delta T_{45}(\text{CLD}) \tag{4b}$$

or,  $T_4 < T_s - 5 \text{ K}$  or  $< T(700 \text{ hPa}) - 5 \text{ K}$ , whichever is lowest. (4c)

Otherwise, the pixel is classified as clear snow/ice. CLD refers to the clear-cloud threshold. The value of the surface temperature  $T_s$  is the first value in the sounding interpolated to the image time. It is assumed that the surface temperature does not vary more than 5 K from the sounding value over the domain. Test (4a) detects most of the clouds, while (4b) identifies most remaining thin cirrus clouds. Test (4c) detects cold clouds. An attempt was made to detect leads, but these were often confused with shadows. Except for (4c), the thresholds for each test were determined through manual inspection of each image and varied from image to image with some dependence on the viewing and illumination angles. Table 1 lists the values for the mean thresholds and their variability for (4a) and (4b). The mean value of  $\Delta T_{34}(\text{CLD})$  decreases from May through July. It should be noted that these values apply only to the area and time of year used in this study.

Over snow, a VIS threshold cannot be used to determine cloudy scenes because the surface and cloudy albedos are similar. Often, as shown in figure 4 for N12 imagery taken at 1936 UTC, 19 May 1998, the clear snow VIS reflectance exceeds the cloudy reflectance. In the middle of the image, the low stratocumulus clouds and the stratus deck to the south are darker than the clear surface. The cloud edges facing the sun are the brightest pixels in the image, while the cloud edges and shadows on the north sides of the thicker stratus clouds are the darkest scenes in the image. The snow surface temperature is also highly variable ranging from black to light gray in the IR temperature image. The locations of the clouds become more obvious in the BTD image in figure 4. In this case, test (4a) finds nearly all of the clouds as seen in the Scene-ID image in figure 4.

An IR threshold may not always be suitable for detecting clouds over snow. In figure 5, an extensive low cloud deck showing some cyclonic structure is up to 7K warmer than the surface in the IR imagery. Although parts of the cloud are brighter than the surrounding snow and ice pack, the VIS reflectance over other portions of the cloud deck is less than it is over all of the surrounding surfaces. Here again,  $\Delta T_{34}$  reveals the location of the clouds (BTD image in figure 5). Some of the apparently open water in this scene, however, is classified as a cloud because it was not dark enough to be classified as clear water. The identification of clouds in the daytime Arctic is considerably improved with the use of  $\Delta T_{34}$  compared to the usual VIS-IR methods.

When a pixel is classified as cloudy, an altitude is assigned to it based on the value of  $T_4$ . In retrievals that include cloud optical depth, it is possible to adjust the observed value of  $T_4$  to account for the semi-transparency of the clouds. If the cloud is optically thick, no adjustment is necessary. Because no optical depths were derived here, the cloud temperature  $T_c$  is assumed to be equivalent to  $T_4$  for all cloudy pixels. The cloud-top height  $z_c$  and pressure  $p_c$  are determined by finding the lowest altitude in the sounding where  $T(z) = T_c$ . The pressure at

altitude  $z$  is also determined from the sounding. The matching procedure begins at the surface and proceeds upward. The clear-sky VIS  $\alpha_{cs}$  and channel-2 albedos were also computed with (2) using the clear pixels.

These analysis procedures were applied to a combined total of 509 images to provide pixel-level retrievals of scene ID, height, and temperature. Mean cloud amounts  $A_c$ , temperatures  $T_c$ , and heights  $z_c$  were computed on a 0.5 latitude by 2° longitude grid for each image. The results falling within 30 min of a given UTC hour were averaged for each month and UTC hour. For comparison with the surface observations, the results from all pixels from a given image within a 25-km radius of the *Des Groseilliers* were averaged to obtain clear-sky albedo and temperature and each of the cloud properties. The mean albedo was computed for each image and averaged using  $\mu_o$  to weight each value. The time-space averaging techniques of *Young et al.* [1998] were applied to fill in the data for each missing hour and to average the values for each month.

#### 4. RESULTS

The distribution of mean clear-sky albedo and temperature  $T_{cs}$  for each month in figure 6 shows a gradient from north to south and an increase from spring into summer as the snow melts and the ice pack breaks up. Areas of open sea appear as the highest temperatures and lowest albedos in the southern portion of the domain. The mean clear-sky VIS albedos vary from only 0.67 to 0.76 during May. Substantial melting in the south during June increases the range from 0.45 to 0.68. The range widens during July from 0.30 to 0.50. Clear-sky temperatures vary by 6 K during May but by only 3 and 4K, respectively during June and July. By July, approximately 8% of the domain was classified as open water. No open water was present during May.

Figure 7 shows the distributions of cloud amount, height, and temperature for each month. Mean cloud amount varies from 52% in the north to 83% in the south during May. The gradient in cloud fraction is nearly east to west during June with a minimum of 55%. By the end of July, the gradient has reversed from the May distribution with minimum cloudiness in the southeastern corner and the maximum across the northern part of the domain. Mean cloud temperatures and heights increase steadily from May through July. Most of the cloudiness during May is below 2 km, while one third of the domain has an average cloud height above 3 km during July.

The monthly mean domain and ship-site cloud properties are listed in Table 2. The mean channel-2 clear-sky albedos (not listed) are 0.593, 0.459, and 0.332 during May, June, and July, respectively. These values are 0.10 less than the corresponding VIS albedos. During May, the AVHRR ship-site clear-sky albedos and temperatures and cloud amounts and heights are very close to the domain average. The cloud temperature is slightly less than the domain average. Except for July, the mean cloudiness at the ship position is close to the average for the entire domain as would be expected from the distribution in figure 7.



Mean cloud amount appears to undergo a fairly regular diurnal cycle during June and July (figure 8). There is a hint of a diurnal signal during May, but it is too small to be significant. The minimum occurs near 0300 LT, while the peak is found between 0900 and 1000 LT. The range is greatest (8%) during July when the surface albedo is lowest for the period. Due to the lack of samples between 1800 and 2400 LT (0500 and 1100 UTC), it can not be determined if there is a semidiurnal cycle or if the cloud amount increases during the late evening.

Figure 9 shows the frequency distribution of cloud-top heights for the entire domain for each month. A quarter of the clouds is found below 500 m while 40% of them occur below 2 km. The remaining clouds are placed between 2 and 6 km with a maximum between 2 and 3.5 km. The distributions are not substantially different from one month to the next, except that during July more extremely low and very high ( $> 4$  km) clouds are observed than during other months.

## 5. DISCUSSION

### a. Cloud amount

To determine how well these results represent the true cloud conditions, it is necessary to understand how they relate to more conventional observations. Here, surface observers' reports from the ship and radar cloud fractions are compared directly with the cloud properties derived within a 25-km radius of the *Des Groseilliers*. Only 80 surface visual observations out of a total of 327 for the surface and 509 from the satellite were taken within 30 min of each other. The mean and standard deviation of the difference between these 80 surface visual observations and the satellite results are 0.020 and 0.123, respectively. The bias represents only a 2.6% relative underestimate of the surface observations, while the rms difference is equivalent to a one-octa uncertainty in the surface observations. If a 3-hr window is used, the bias and rms difference increase to 0.038 and 0.144, respectively, for 327 points. For clouds as low as those in this domain, a 25-km radius may be too large to accurately represent the distance observed from the surface.

The average cloud fractions from the surface observers for each month are 73.3, 71.5, and 80.7% for May, June, and July, respectively, if obscured observations due to drizzle, snow, and fog are not included. If it is assumed that these obscured cases are actually overcast, then the respective monthly mean *Des Groseilliers* cloud amounts rise to 76.3, 76.0, and 86.7%. Thus, the mean AVHRR-derived cloud amounts over the ship (Table 2) are in good agreement with the surface observations for June and July. However, it appears that the satellite analysis underestimates the May total cloud cover by 3-6%. Considering the range in observations for the entire period due to the unknown cases, the satellite cloud amounts are either 1.3% too high or 3% too low.

Another way to evaluate the satellite results is to determine if the distribution of cloud amounts from the two datasets are comparable. The AVHRR cloud amounts were binned according to octas to match the cloud amounts observed from the surface. Cloud amounts less

than 2% were assumed to be clear (zero octas), while the  $2 < A_c < 18.75\%$  are included in the first octa. The selection of the limited cloud amount for the clear case is based on the small number of pixels that are classified as clouds in an otherwise clear scene simply because the  $T_3$  striping affected the clear-sky BTD. Most ship-centered satellite analyses produced at least a few cloudy pixels. An octa of 8 is assumed to correspond to  $A_c > 93.75\%$ . An equal spacing of 12.5% is assumed for the intervening octas. Figure 10 shows that the surface and satellite frequency distributions of cloud amounts are very similar. In both cases, approximately 55% of the scenes are overcast (8 octas). The surface observer also sees twice as many 7/8 cloudy skies as the satellite and less than half the amount of clear skies. Examination of some of the cases indicates that the surface viewer detects partly cloudy conditions in some optically thin cloud cases where the satellite sees little or no cloudiness. As indicated below, the radar detects overcast conditions in these same cases. These conditions may explain the satellite underestimates during May relative to the ship.

To minimize noise in the radar-derived cloud amounts, cloud fraction was computed by using only those cloud returns that persisted more than 5 min in the radar image and by eliminating all times when there were a few minutes of data drop out. The results are compared with the satellite and surface-observer cloud-amount frequencies for four categories in Table 3. There is excellent agreement between all three datasets for most clear and overcast conditions. The greatest discrepancies occur in the last row of the table where the radar detects an overcast scene, while the satellite and surface observer see significantly less cloudiness 22 and 18% of the time, respectively.

Examination of the radar data reveals that, in many of these cases, the radar detects a physically thick, but apparently optically thin, high cloud layer or some diamond dust at low levels that produces returns with intensities smaller than -25 dBz. In a few cases, higher intensities occur periodically within the cloud deck as seen in figure 11 for May 21. The surface observer detects some clouds in these instances, but does not interpret the layer as overcast because of some very thin parts. The satellite image for 1628 UTC in figure 12 shows the variability in these high clouds. Shadows cast by the almost linear thick portions of the clouds are evident in the VIS image. The areas between the obvious clouds appear to be clear in the IR image. Inspection of the BTD image in figure 12, however, reveals more high cloudiness than seen in the IR image, but many of the  $\Delta T_{34}$  values are only about 3K, well below the cloud detection threshold. In this case, the cold cloud test finds most of the cloud layer seen by the radar because  $T_4$  is 10K colder than the surface. The observer on the ship cannot see most of these clouds and they are nearly transparent in the IR data. Thus, it is assumed that they are subvisual clouds with extremely small optical depths. From these subjective and objective comparisons it is concluded that, except for subvisual clouds, the current analysis of AVHRR data yields cloud amounts that, on average, are within 3% of those seen from the surface for clouds.

The diurnal variation in mean cloud amount from the ship observations is characterized by a 7% range during each month. During May and June, the maximum occurs between 0700 and 1300 LT, a period similar to that for the domain maxima seen in figure 8. During July, however, the ship observations show a minimum at 0700 LT and a maximum at 1900 LT. The satellites did not observe the domain after 1800 LT, so the linear interpolation used to fill in missing hours would have missed the maximum. The difference between the satellite and surface observations for July, however, is most likely due to the ship position. During May and June, the ship observations were very close to the domain averages. However, during July, the ship was further north and the cloud characteristics were different from the domain averages. Another source of discrepancy is the sparse 6-hourly sampling from the surface. The four local times do not provide a very detailed picture of the diurnal cycle.

The diurnal variations observed for the domain could be the result of increased solar warming of the surface during the day as the solar altitude rises as seen over many land areas during the summer. The surface heating would induce some convection and increase evaporation within the boundary layer during the day. The increase in the amplitude with time may be due to the rapidly decreasing surface albedo from May to July. Although the diurnal change of insolation is similar, the high albedo during May prevents much surface absorption. Unlike ocean areas, the water that absorbs the solar radiation is in shallow ponds on the ice surface so that more sensible heat would be available for convection. Further analysis of possible convection leading to a diurnal cycle in the boundary layer cloudiness is needed.

#### *b. Cloud top altitude*

Cloud-top heights from AVHRR were matched with the radar data for all single-layer cloud cases with  $A_c > 90\%$  to provide a clean comparison. The results plotted in figure 13 show that the cloud top from the AVHRR retrieval agrees extremely well for the low cloud cases and for some of the higher clouds. Most of the high-cloud tops are underestimated by an average of 2 km, presumably because they are optically thin and no emissivity corrections were applied. The mean altitude difference is 0.8 km with a standard deviation of 1.8 km. Most of the higher clouds are also physically thick and nebulous so that the mean radiating temperature is probably representative of some level near the center of the cloud. Thus, corrections for semitransparency may not bring the satellite and radar cloud tops into complete agreement for these cases. Conversely, the satellite retrieval overestimates cloud-top height relative to the radar retrieval for some clouds below 2000 m. These clouds appear slightly colder than coldest temperature under the surface layer inversion and are placed 2 km higher. To simplify the retrievals, the SHEBA soundings were reduced in resolution so that some of the more extreme temperatures under the inversions may have been eliminated. Thus, the cloud would be placed higher in the atmosphere where the temperature occurs again. Future retrievals should use the best available soundings to ensure proper cloud top placement.

Cloud layering may also affect the determination of cloud heights. For example, if it is assumed that a high thin cloud occurs over a thick cloud, then the satellite will see some of the radiance from the thick cloud through the thinner one. The resulting cloud height will be somewhere between the two. To see how such an effect would alter the cloud height distribution, cloud height histograms from the radar were constructed in two ways. In one case, the highest cloud top height was counted whether it occurred with a cloud below it or not. Thus, in a multilayer cloud, only the highest cloud-top height counted as one occurrence. In the second case, the cloud-top heights were averaged for multilayer clouds. The results are shown in figure 14. In figure 14a, the histogram for individual clouds shows a high frequency of clouds above 5 km. The averaged cloud-top heights in figure 14b are more frequent between 3 and 6 km with far fewer clouds occurring at altitudes above 6 km. This latter histogram is more like that in figure 9 than is figure 14a. The satellite, however, detects far fewer clouds above 6 km than either averaging method. Thus, it is clear that both semitransparency and overlapped clouds must be taken into account to achieve accurate remotely sensed cloud heights from AVHRR data.

### *c. Climatology*

Few long-term surface observations of cloud amounts are available for the Arctic, although some average values for 1952-81 are reported for a few Arctic locations in the surface cloud observation atlas of Warren *et al.* [1988]. Their mean total cloud amounts for the area between 140 and 165°W and 75 and 87°N for that period are 73, 81, and 85% during May, June, and July, respectively. While the seasonal trends are similar to the AVHRR observations, the magnitudes are 5 - 10% greater than the domain averages in Table 2 and close to the magnitudes derived from the *Des Groseilliers*.

The ISCCP satellite observations probably constitute the longest, recent record of cloud amounts for this area. Average cloud properties were computed using the D2 results from May and June 1984 through 1994 and from July 1983 through July 1994 for the area encompassed by 72.0 - 80.0°N and 130 - 170°W. The cloud amounts are between 15 and 30% less than those from the earlier surface climatology and do not exhibit an increase as summer proceeds. This difference between the ISCCP amounts and the surface climatology is similar to the differences reported by Schweiger *et al.* [1999] for a different portion of the Arctic using ISCCP D2 and ship data taken during 1990. If it is assumed that the cloud variability in the ISCCP dataset is a true reflection of the interannual variations that would be observed from the surface, then the *Des Groseilliers* averages are within one ISCCP standard deviation of the means from Warren *et al.* [1988]. Thus, it can be concluded that the mean cloud amounts during FIRE ACE are typical for that part of the Arctic even though the extent of the ice pack in the Beaufort and Chukchi Seas reached a record minimum during July 1998 [Maslanik *et al.* 1999].

The surface albedos from ISCCP can be compared with those from the current analysis by correcting the domain TOA VIS albedos in Table 2 for ozone absorption and Rayleigh scattering. The TOA VIS albedo was computed as a function of Lambertian surface albedo using

the adding-doubling model of Minnis et al. [1993] at 0.65  $\mu\text{m}$ . The computations assume an ozone optical depth of 0.030 and account for Rayleigh scattering. The domain values in Table 2 yield surface albedos of 0.82, 0.72, and 0.60 for May, June, and July, respectively. Except for June, when the current value is 0.05 less than the ISCCP result, there is good agreement between these results and the 11-year means suggesting that the composition of the surface (i.e., snow, ice, ponds, etc.) is fairly typical for this domain. During May, the domain clear-sky temperature is 2 K greater than the ISCCP mean, a value that is slightly larger than the standard deviation. During June, the FIRE ACE  $T_{cs}$  is within the interannual variation derived from the ISCCP data. However, during July,  $T_{cs}$  is 2.4K less than the ISCCP mean, a difference equal to 2 standard deviations.

Cloud amounts are 11, 19, and 13% greater in this study than the corresponding ISCCP means for May, June, and July, respectively. The cloud amount differences are discussed below. Cloud-top pressure and temperature are 40 hPa and 2K greater, respectively, from the current analysis than from the ISCCP mean for May. This difference is typical for the entire period. The value of  $T_c$  is within one standard deviation of the ISCCP mean only for May. The temperature and pressure differences may be due to the detection of more low clouds here or to the lack of an optical depth correction. It is not clear how often optically thin clouds were detected by the ISCCP in this area. Overall, both the clear and cloudy temperatures are 2K warmer than that observed by ISCCP suggesting either an IR calibration difference or greater-than-usual warming during May. Only the cloud temperatures were 2 K warmer than the ISCCP average during the other months.

The ISCCP D1 results provide 3-hourly cloud parameters on a 250-km scale. Over the Arctic, past NOAA satellites have taken data at all hours of the day. The 3-hourly averages between 1984 and 1994 have a maximum at 1000 LT (2100 UTC) and a minimum around 2200 LT. The ranges vary from 19 to 34% for the 3 months. The spatial coverage between 0600 and 1200 UTC is much less than that for the other hours so the averages may not be as representative at those hours. For the same hours sampled in this study, the diurnal ranges in the ISCCP cloud averages vary from 8-10%, similar to the values found here. Thus, both the phase and range in mean cloud amount during FIRE ACE is consistent with past measurements and the contemporaneous ship observations.

#### *d. Current vs. ISCCP analyses*

It has been shown that the retrieval method applied here yields more accurate cloud amounts than obtained using the ISCCP D version for cloud detection [Rossow *et al.* 1996] compared to surface observations. Both techniques used the same general approach to cloud detection using AVHRR data. The difference primarily relies on the threshold selection values and the input data used to set the thresholds. ISCCP uses a fixed BTD threshold of 8K or the difference that is equivalent to a SI reflectance of 0.055 for all cases, while the current method used subjectively determined BTD thresholds that vary depending on the scene. The same

approach cannot be used in an operational mode because the volume of data precludes a subjective analysis. Additionally, the ISCCP relies on a composite map gathered over several weeks to determine the clear-sky temperatures for IR threshold determination. The current analysis used relatively high temporal resolution soundings to provide temperatures at the surface and 700 hPa to set the IR threshold. The compositing approach provides a highly uncertain clear-sky temperature (e.g., *Schweiger et al.* 1999) in the Arctic because of the initial difficulty in screening clouds to find clear scenes. The ISCCP also does not have the luxury of having the high-resolution soundings available during FIRE ACE.

Perhaps the sounding problem could be mitigated to some extent by employing an IR threshold corresponding to some selected altitude above the surface using the temperature from the ISCCP TOVS sounding or some other atmospheric profile source as used here. The variability of the SI threshold may be taken into account by using a SI bidirectional reflectance model of a simulated snow surface like that employed by *Han et al.* [1999] for the VIS channel. An example of such a model is shown in figure 15a that plots the results of reflectance calculations with an adding-doubling model [*Minnis et al.* 1993] for an ice cloud with an optical depth of 1000 and temperature of 260K. Optical properties for a hexagonal ice column 750- $\mu\text{m}$  long and 160- $\mu\text{m}$  wide [*Minnis et al.* 1998] were used to simulate large snow crystals. Over the range of solar zenith angles in the Arctic, the SI reflectance remains below 0.02 for all azimuth angles but direct forward scattering and for  $\theta < 60^\circ$ , except when  $\theta_o = 82.1^\circ$ . Most useful data are taken at  $\theta < 60^\circ$ . The corresponding BTD values shown in figure 15b vary from 2 to 6K for the assumed surface (cloud) temperature for  $60^\circ \leq \theta_o \leq 82.4^\circ$ . These values are very close to the mean values computed from the clear scenes for May. The mean domain value for May was 4.4K for an average value of  $\theta_o = 71.1^\circ$ . It ranged from 2.8 to 5.7K depending on  $\theta_o$ . The empirical thresholds suggest that the variation is nearly as large as the reflectance itself.

The reflectances in figure 15a vary with the angles indicating that biases in cloud detection would occur as a function of viewing and illumination angles if a fixed reflectance threshold is used. Because it corresponds to more than twice the current values in Table 1, the ISCCP BTD threshold would likely classify more cloudy pixels as clear than the present method. As the surface temperature rises, the average BTD for clear snow will decrease because of the extremely non-linear variation of radiance with temperature at 3.7  $\mu\text{m}$ . This change is consistent with the decreasing thresholds for June and July in Table 1. While a method using a model like that in figure 15a may be more realistic, it may have difficulty accounting for reflectance variability when the surface becomes slushy or contains ponds that reduce the albedo as seen in the VIS channel for June and July (Table 2). Thus, any model applied in an automated method may need to be more sophisticated than the simple one-crystal calculation demonstrated here.

#### *e. Warm clouds*

Most of the clouds in figure 5 are warmer than the surface, while some are the same brightness or darker than the surface in the VIS channel. Without the BTD technique, it would be extremely difficult to detect all of these clouds even with a sounding approach like the 3I method because of the obviously strong inversion associated with this warm cloud. Figure 16 shows two soundings, one prior to the passage of this warm cloud deck over the SHEBA camp at 2315 UTC, 20 July and another at 1718 UTC, 21 July when the cloud deck was above the site. The thinner, lower clouds reached the camp around 0500 UTC and had thickened to 800 m by 1200 UTC. The cloud deck took ~18 hours to pass over the camp. The first sounding shows a strong inversion from the surface to 400 m. The relative humidity  $RH$  at the surface is nearly 100%. A humidity inversion then occurs at 1500 m, while the temperature lapse rate is fairly constant above 400 m. After the cloud deck rolled in, the atmospheric structure became more complex with an inversion base at 100 m above the surface, another change in lapse rate at 300 m to a much stronger positive lapse rate to 800 m, the top of the boundary layer inversion. The air is saturated up to 600 m. Relative humidity decreases to 80% at the top of the inversion, then remains constant up to 2000 m. The radar places the cloud top at 800 m and the base near the surface.

This entire cloud exists in air that is very stable and moist with a top that is 10 K warmer than its base. This structure suggests that it is like a deep advection fog produced by warm air from the south that was moistened and cooled by passage over the open water but trapped by the strong inversion. As it passed over the ice pack, it must have cooled more at the base causing a deepening of the cloud. The cloud mass has a cyclonic appearance in the imagery of figure 5 and figure 17 indicating the formation of an organized system underneath the inversion. The origin of clouds like these that are difficult to detect with standard IR thresholds is beyond the scope of this paper, but it is an interesting aspect that could shed some light on the nature of Arctic cloud systems.

The SHEBA soundings show that during May, more than 90% of boundary layers had a structure similar to that in figure 16 for 21 July where the base of the inversion is elevated. During June, almost half of the inversions begin at the surface like that for 20 July in figure 16. The number of surface inversions is only 30% during July. The strength of the inversions during June and July may have contributed to the lower-than normal cloud cover.

#### *f. Near-infrared cloud detection*

Summertime Arctic clouds should become easier to detect with future satellite systems because of the availability of near-infrared channels that use wavelengths near 1.6 or 2.1  $\mu\text{m}$ . The new series of AVHRR instruments are designed with a variable channel 3 that can operate at 1.6 or 3.75  $\mu\text{m}$  depending on the solar illumination. Figure 17 shows the 1.6- $\mu\text{m}$  image from the NOAA-15 AVHRR taken 3 hours after the N12 image in figure 5. The cloud systems are significantly more reflective than either the ice pack or open water making identification of the

clear areas simpler than possible with the AVHRR channels used here. The NOAA-15 1.6- $\mu\text{m}$  channel was only available for a short time before the 3.75- $\mu\text{m}$  channel was turned on permanently. Calibration difficulties and limited temporal coverage excluded its use in this study.

## **6. CONCLUDING REMARKS**

Based on the comparisons with ground truth data, the cloud amounts derived here accurately represent the cloudiness that occurred over the greater SHEBA domain during the FIRE ACE period. The detailed subjective threshold determinations were an essential factor in achieving the good agreement with surface observations. Better objective cloud detection for automated methods like that used by the ISCCP may be accomplished by implementing a BTDR threshold that depends on the viewing and illumination angles as well as the surface VIS albedo. Otherwise, summertime Arctic cloud amounts will be underestimated using VIS, IR, and SI channels only.

The cloud amounts and surface properties observed during FIRE ACE appear to be typical of the conditions in the Arctic during summertime with maximum cloudiness during July. Thus, any conclusions drawn from studies of clouds during FIRE ACE should be generally representative of summertime Arctic clouds in this area. Low clouds are the dominant cloud type and will occasionally be warmer than the surface. Mean cloud amount varies diurnally with a peak a few hours before local noon and a range of  $\sim 10\%$ . The cloud-top heights derived from the satellite are within a few hundred meters of the radar-determined values for the low clouds. Because no corrections were applied to account for optical depth, the cloud-top heights for clouds above 2000m are underestimated by 2000m on average. However, because these high clouds were often physically thick, the cloud heights from the satellite are actually close to the cloud center altitude. These results should be valuable for improving the modeling of meso-scale Arctic cloud systems.

The information derived here can also be used to develop improved automated techniques for Arctic cloud detection. Further scene identification is being developed to determine (cloud) shadowed or lead pixels. Because leads are often evident in cloudy parts of the VIS image, it may not be necessary to find clear scenes to detect leads. The algorithms applied in this study yield only basic information about the FIRE ACE clouds. Additional research is needed to refine these algorithms for automatic application and for deriving other cloud properties like optical depth, phase, and particle size. Still more improvement in Arctic cloud detection will come with the availability of near-infrared sensors on the upcoming AVHRRs and the imagers on the Earth Observing System satellites, Terra and Aqua. With all of those refinements, it will be possible to obtain a more complete picture of clouds and their role in the radiation budget of the Arctic.



## Acknowledgments.

Special thanks are reserved for Bill Smith, Jr., Mandy Khaiyer, Pat Heck, Kirk Ayers, Shalini Mayor, Jeff Otten, and Duane Hazen for monitoring and collecting the data during FIRE ACE. Thanks to David Young for proofing the manuscript and to Yongxiang Hu for his advice on snow modeling. This research was supported by NASA Earth Sciences Enterprise Radiation Sciences Program FIRE Project and by the Environmental Sciences Division of the U.S. Department of Energy Interagency Agreement DE-AI02-97ER62341 as part of the Atmospheric Radiation Measurement (ARM) Program sponsored by the Office of Science, Office of Biological and Environmental Research, Environmental Sciences Division. The ship data were also obtained from the ARM Program and from the NSF-SHEBA program under agreement #OPP-9701730.

## References

- Chedin, A., N. A. Scott, C. Wachiche, and P. Moulinier, The improved initialized inversion method: A high resolution physical method for temperature retrievals from the TIROS-N series. *J. Clim. Appl. Meteorol.*, **24**, 124-143, 1985.
- Clothiaux, E. E., T. P. Ackerman, G. G. Mac, K. P. Moran, R. T. Marchaud, M. A. Miller, and B. E. Martner, Objective determination of cloud heights and radar reflectivities using a combination of active remote sensors at the ARM CART sites. Accepted *J. Appl. Meteorol.*, 1999.
- Curry, J. A., W. B. Rossow, D. Randall, and J. L. Schramm, Overview of Arctic cloud and radiation characteristics. *J. Climate*, **9**, 1731-1764, 1996.
- Curry, J. A., P. Hobbs, M. D. King, D. Randall, P. Minnis, T. Uttal, G. A. Isaac, J. Pinto, et al. FIRE Arctic Clouds Experiment. In press, *Bull. Am. Meteorol. Soc.*, 1999.
- Doelling, D. R., P. Minnis, C. Venkatesan, A. Mahesh, F. P. J. Valero, and S. Pope, Cloud radiative forcing during FIRE ACE derived from AVHRR data. Submitted to *J. Geophys. Res.*, this issue, 1999.
- Han, W., K. Stamnes, and D. Lubin, Remote sensing of surface and cloud properties in the Arctic from AVHRR measurements. *J. Appl. Meteor.*, **38**, 989-1011, 1999.
- Key, J. and R. G. Barry, Cloud cover analysis with Arctic AVHRR data 1. Cloud detection. *J. Geophys. Res.*, **94**, 18,521-18,535, 1989.
- Maslanik, J. A., M. C. Serreze, and T. Agnew, On the record reduction in 1998 western Arctic sea-ice cover. *Geophys. Res. Lett.*, **26**, 1905-1908, 1999.
- Minnis, P., D. P. Garber, D.F. Young, R. F. Arduini, and Y. Takano, Parameterization of reflectance and effective emittance for satellite remote sensing of cloud properties. *J. Atmos. Sci.*, **55**, 3313-3339, 1998.
- Minnis P. and E. F. Harrison, Diurnal variability of regional cloud and clear-sky radiative parameters derived from GOES data; Part I: Analysis method. *J Climate Appl. Meteorol.*, **23**, 1032-1052, 1984.
- Minnis, P., Y. Takano, and K.-N. Liou, Inference of cirrus cloud properties using satellite-observed visible and infrared radiances, Part I: Parameterization of radiance fields. *J. Atmos. Sci.*, **50**, 1279-1304, 1993.
- Nguyen, L., P. Minnis, J. K. Ayers, W. L. Smith, Jr., and S. P. Ho, Intercalibration of geostationary and polar satellite data using AVHRR, VIRS, and ATSR-2 data. *Proc. AMS 10<sup>th</sup> Conf. Atmos. Rad.*, Madison, WI, June 28 – July 2, 405-408, 1999.
- Perovich, D. K., E. L. Andreas, J. A. Curry, H. Elken, C. W. Fairall, T. C. Grenfell, P. S. Guest, J. Intrieri, et al., Year on ice gives climate insights. *Eos*, **80**, 481-486, 1999.
- Rao, C. R. N., and J. Chen, 1996: Post launch calibration of the visible and near-infrared channels of the Advanced Very High Resolution Radiometer on NOAA-14 spacecraft. *Intl Jour. Remote Sens.*, **17**, 2743-2747, 1996.

- Rossow, W. B. and R. A. Schiffer, Advances in understanding clouds from ISCCP. *Bull. Am. Meteorol. Soc.*, **80**, 2261-2287, 1999.
- Rossow, W. B., A. W. Walker, D. Beuschel, and M. Roiter, International Satellite Cloud Climatology Project (ISCCP): description of new cloud datasets. WMO/TD-No. 737, World Climate research Programme (ICSU and WMO), Geneva, Switzerland, 115 pp., 1996.
- Schweiger, A. J., R. W. Lindsay, J. R. Key, and J. R. Francis, Arctic clouds in multiyear datasets. *Geophys. Res. Lett.*, **26**, 1845-1848, 1999.
- Stubenrauch, C. J., W. B. Rossow, F. Cheruy, A. Chedin, and N. A. Scott, Clouds as seen by satellite sounders (3I) and imagers (ISCCP). Part I: Evaluation of cloud parameters. *J. Climate*, **12**, 2189-2213, 1999.
- Suttles, J. T., R. N. Green, P. Minnis, G. L. Smith, W. F. Staylor, B. A. Wielicki, I. J. Walker, D. F. Young, V. R. Taylor, and L. L. Stowe, Angular radiation models for Earth-atmosphere system: Volume I - Shortwave radiation. *NASA RP 1184*, 144 pp., 1988.
- Warren, D., AVHRR channel-3 noise and methods for its removal. *Int.J. Remote Sensing*, **10**, 645-651, 1989.
- Warren, S. G., C. J. Hahn, J. London, R. M. Chervin, and R. Jenne, Global distribution of total cloud cover and cloud type amounts over the ocean. *NCAR Technical Note TN-317+STR*. Boulder, Colorado, 1988.
- Young, D. Y., P. Minnis, D. R. Doelling, G. G. Gibson and T. Wong, Temporal interpolation methods for the Clouds and the Earth's Radiant Energy System (CERES) Experiment. *Jour. Appl. Meteor.* **37**, 572-590, 1998.

Table 1. Normalization coefficients for NOAA-12 AVHRR channels 1 and 2.

Month	$\Delta T_{34}(\text{CLD}), \text{K}$	, K	$\Delta T_{45}(\text{CLD}), \text{K}$	, K
May	8.6	1.8	1.5	0.3
June	5.7	1.3	1.5	0.3
July	5.4	2.6	1.5	0.3

Table 2. Mean cloud and surface parameters derived from AVHRR data for the study domain during 1998.

Month	$T_{cs}$ (K)		$\alpha_{cs}$		$A_c$ (%)		$T_c$ (K)		$z_c$ (km)	
	ship	Domain	ship	Domain	ship	Domain	ship	Domain	ship	Domain
May	264.0	263.9	0.695	0.709	70.5	70.1	257.5	259.1	2.2	1.9
June	269.9	268.4	0.573	0.556	75.2	73.6	262.0	263.5	1.6	2.3
July	270.1	271.0	0.497	0.430	84.4	69.4	264.1	265.4	2.8	2.6

Table 3. Frequency of cloud amounts in percent from radar, AVHRR, and surface observations at the *Des Groseilliers*, May - July 1998.

Radar	AVHRR A <sub>c</sub> (%)				Ship Observer A <sub>c</sub> (%)			
A <sub>c</sub> (%)	0 - 15	15 - 50	50 - 85	85 - 100	0 - 15	15 - 50	50 - 85	85 - 100
0 - 15	7	1	0	1	9	4	0	1
15 - 50	1	1	1	1	1	1	1	1
50 - 85	1	1	1	1	0	0	2	2
85 - 100	5	5	12	61	1	5	12	60

Table 4. Mean and standard deviations of ISCCP D2 cloud properties for 1983-1994 for 72.5 - 80.0°N and 130 - 170°W.

Property	May		June		July	
	mean		mean		mean	
$A_c$ (%)	58.9	8.9	55.1	7.0	56.8	9.5
$p_c$ (hPa)	710.2	31.9	714.5	14.5	650.0	20.4
$T_c$ (K)	257.0	2.1	261.7	1.1	262.0	1.8
$\alpha_s$	0.83	0.02	0.74	0.03	0.61	0.03
$T_{cs}$ (K)	262.2	1.3	269.5	0.7	272.5	1.2

## FIGURE CAPTIONS

Figure 1. Analysis domain and position of *Des Groseilliers* during FIRE ACE from 1 May to 31 July 1998.

Figure 2. Sampling pattern of NOAA-12 and NOAA-14 over the SHEBA ice camp during May 1998.

Figure 3. Scatterplot of co-angled, collocated brightness counts from the NOAA-12 and NOAA-14 channels 1 and 2 for May 1998 over the western Arctic Ocean. Regression-fit lines are also shown.

Figure 4. Visible, infrared, BTM, and Scene-ID images for N12 data taken at 1936 UTC, 19 May 1998.

Figure 5. Same as figure 4, except for 0251 UTC, 21 July 1991.

Figure 6. Distribution of mean clear-sky VIS albedos and IR temperatures derived from AVHRR data during FIRE ACE.

Figure 7. Distribution of mean cloud amounts, temperatures, and heights derived from AVHRR data during FIRE ACE.

Figure 8. Diurnal variation of monthly mean cloud amount over the domain.

Figure 9. Distribution of cloud-top heights from the satellite retrievals.

Figure 10. Frequency distribution of cloud amount from the *Des Groseilliers* surface observers and from AVHRR data within a 25-km radius of the ship during FIRE ACE.

Figure 11. MMCR image from the *Des Groseilliers* from 1200-2400 UTC, 21 May 1998. Percentages at top are satellite-derived cloud amounts. Fractions in red are surface-observed cloud amounts.

Figure 12. Same as figure 4, except for 1628 UTC, 21 May 1998. Note striping in BTM image.

Figure 13. Scatterplot of cloud-top heights from the *Des Groseilliers* MMCR and the AVHRR retrievals during FIRE ACE. The regression-fit (solid) and agreement (dashed) lines are also plotted.

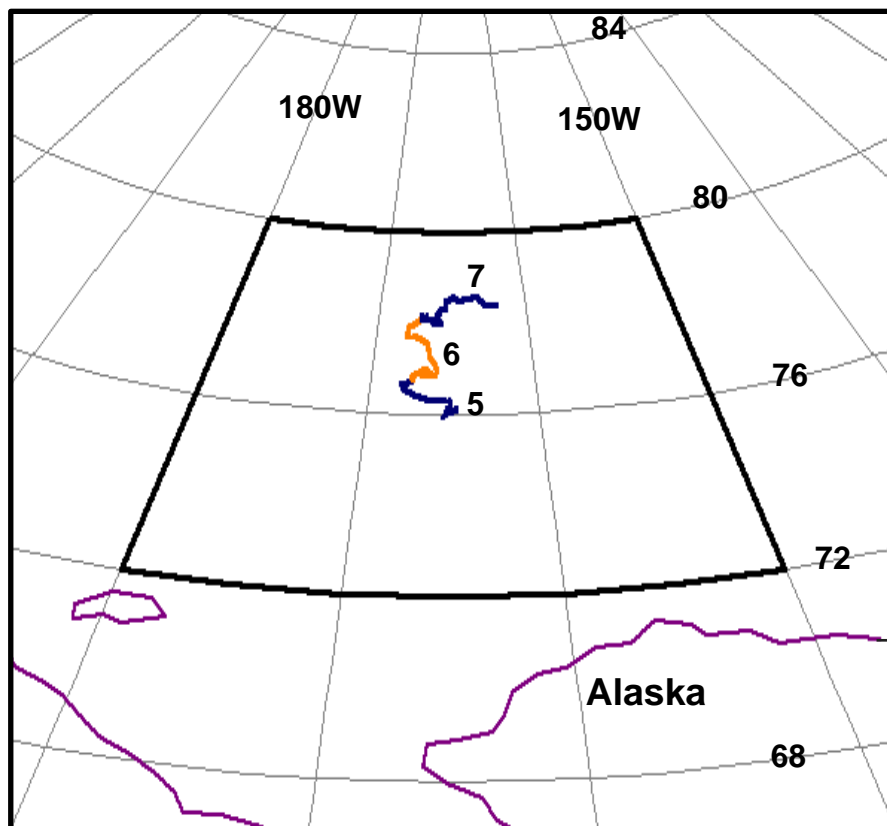


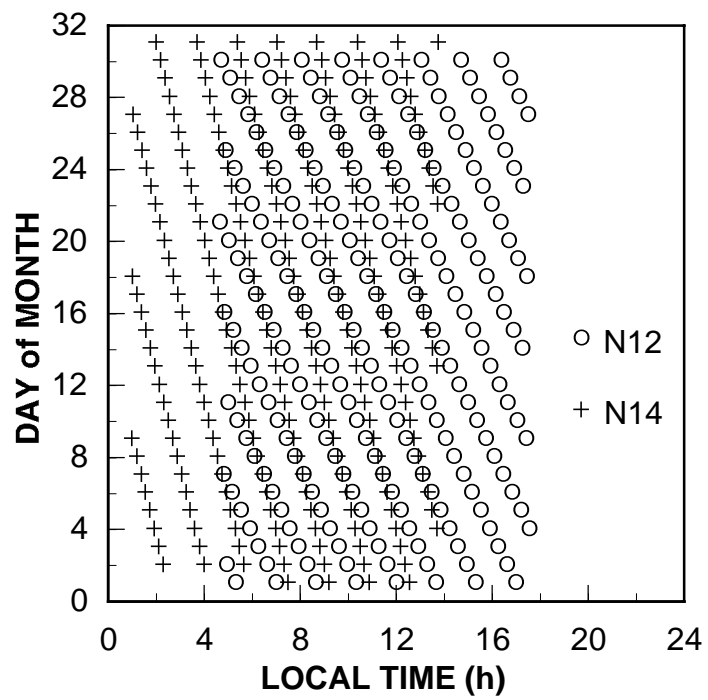
Figure 14. Histograms of cloud-top heights from the SHEBA MMCR during May-July 1998.

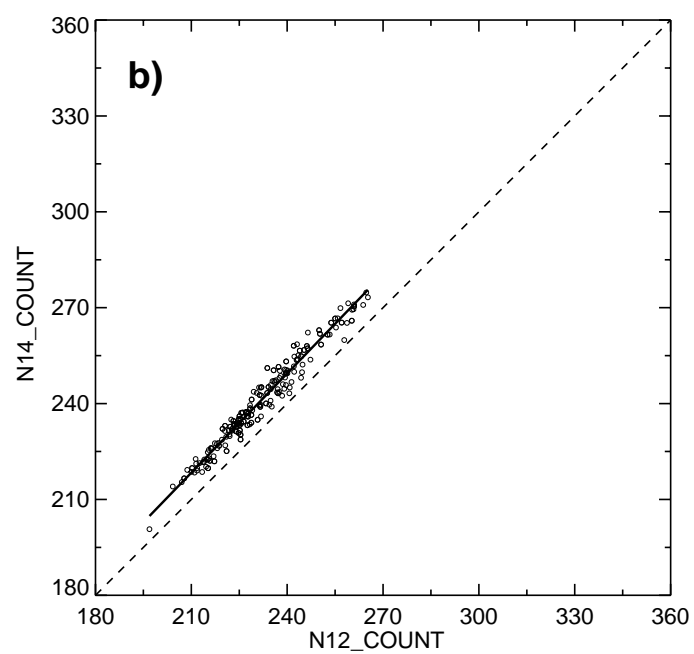
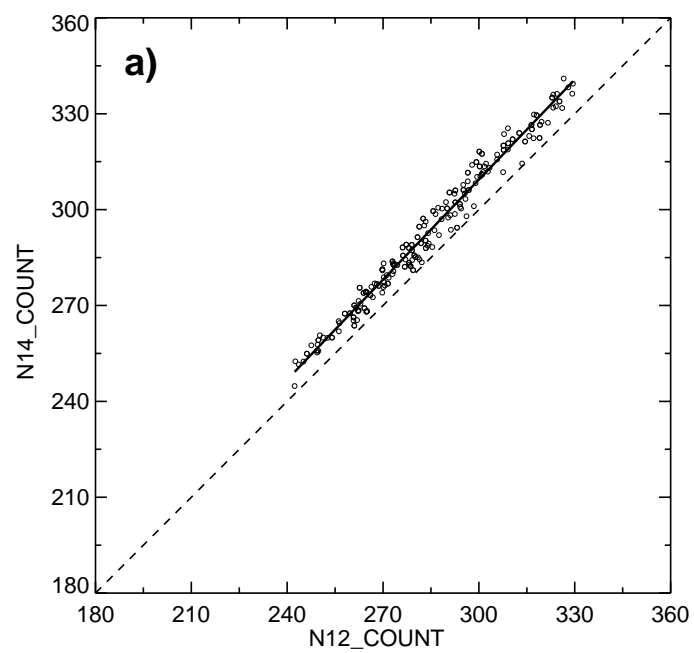
Figure 15. Simulation of snow (a) 3.75- $\mu\text{m}$  reflectance and (b)  $\Delta T_{34}$  from theoretical calculations using a hexagonal ice crystal cloud with an optical depth of 1000 at  $T_c = 250\text{K}$ .

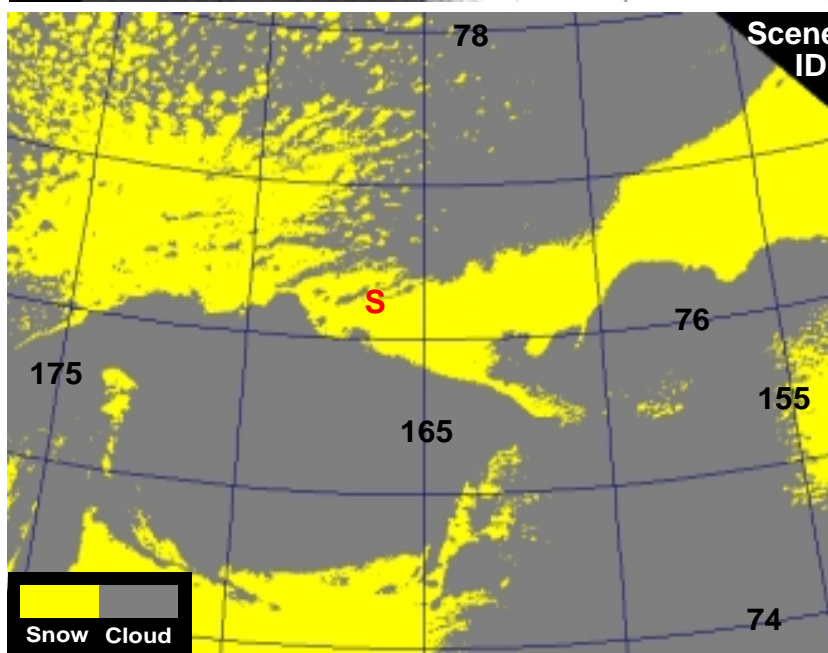
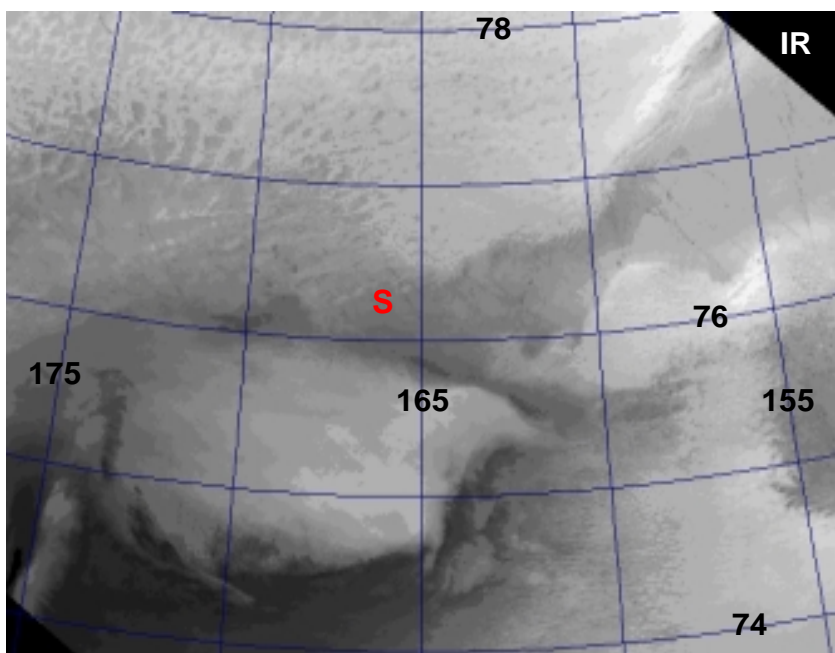
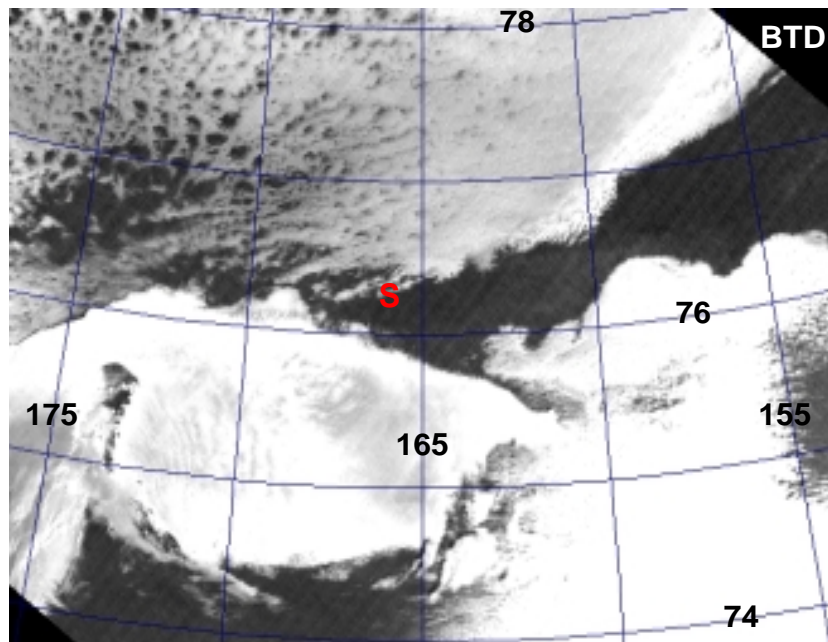
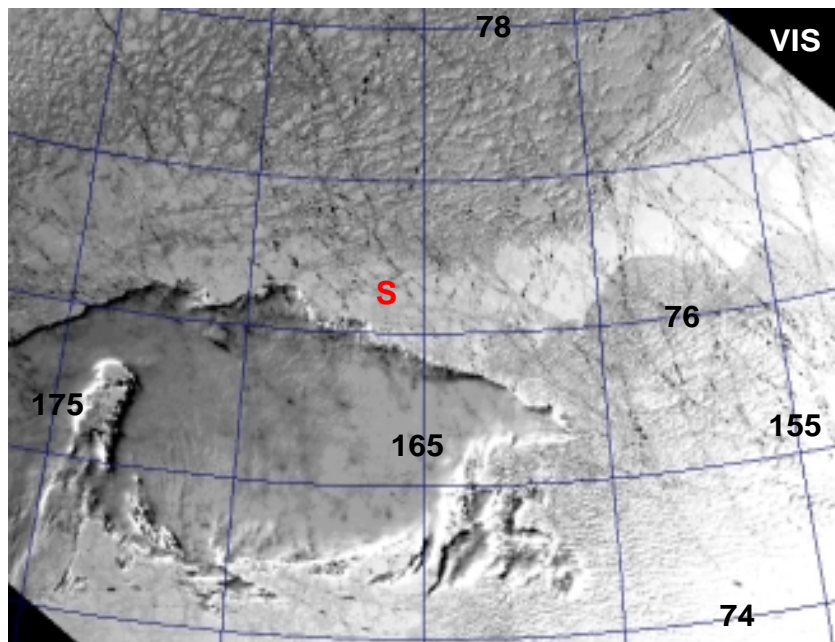
Figure 16. Temperature profiles from rawinsondes launched from the *Des Groseilliers* during FIRE ACE.

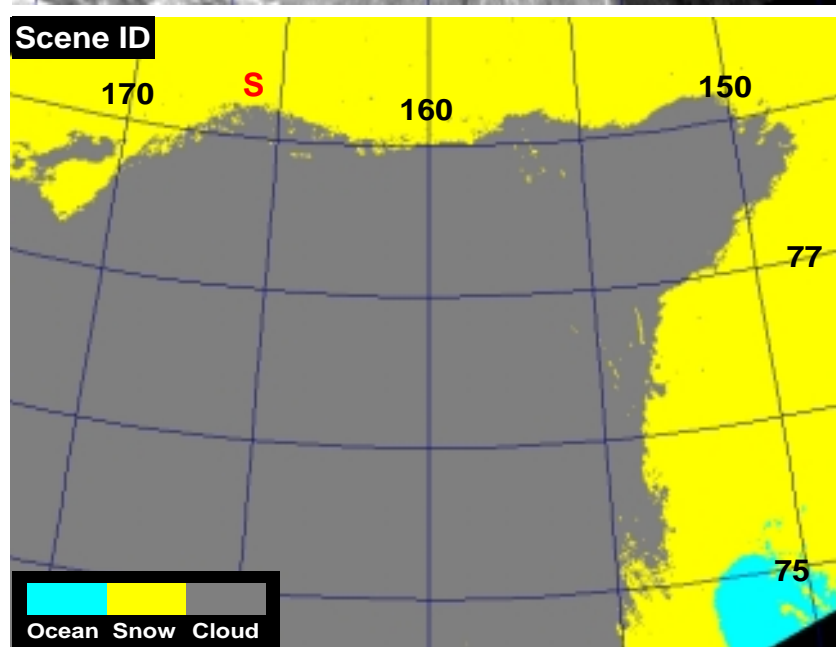
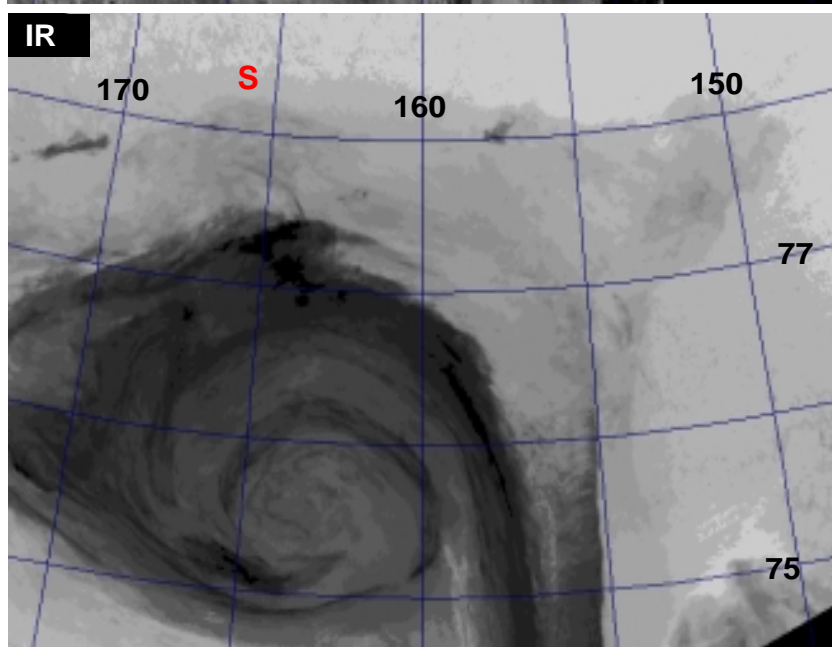
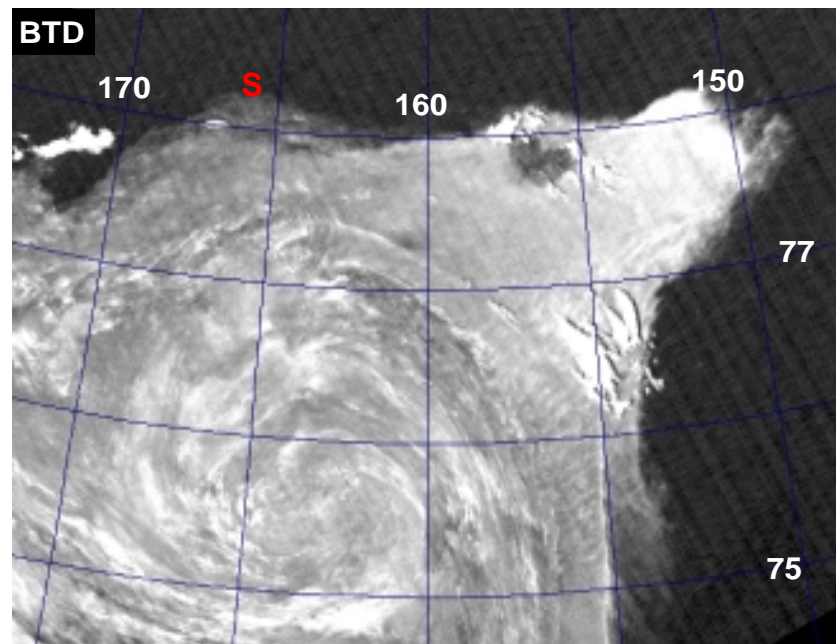
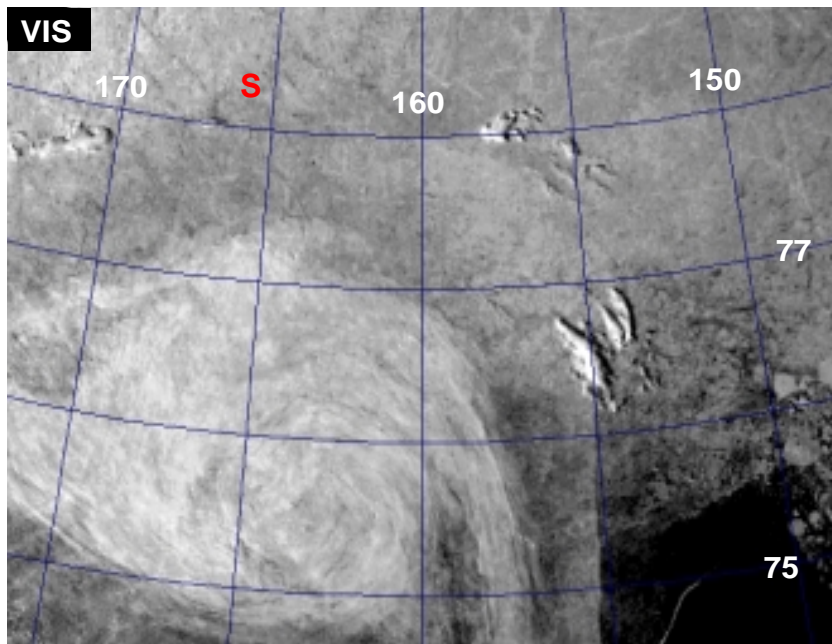
Figure 17. NOAA-15 AVHRR imagery taken over the Arctic at 0513 UTC, 21 July 1998. The false color 3-channel overlay (red=VIS, green = 1.6  $\mu\text{m}$ , blue= IR) was created using histogram equalization to enhance differences between snow (pink), clear water (dark blue), thick water cloud (white), ice clouds (light blue/gray), and thick clouds over various backgrounds.

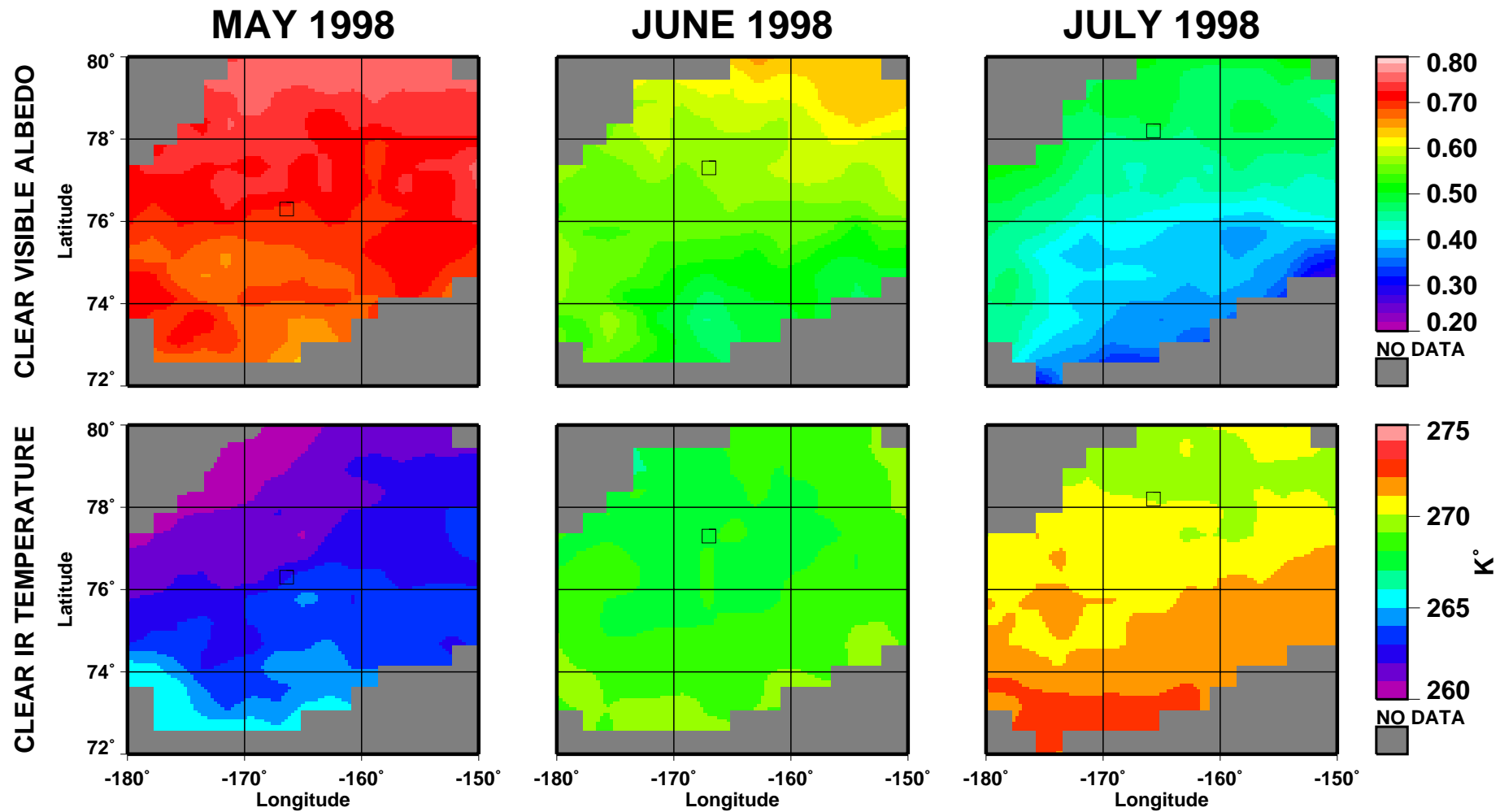


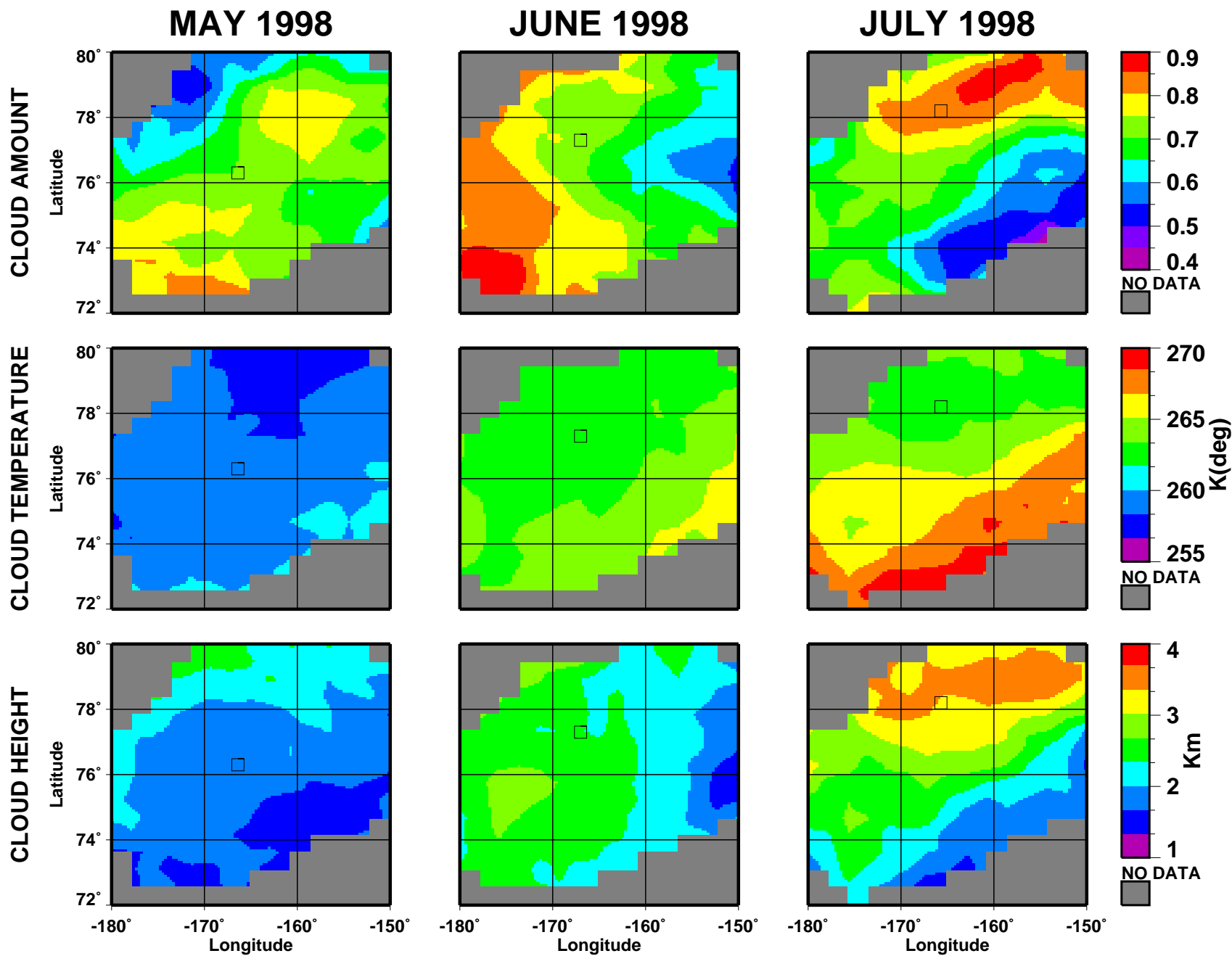




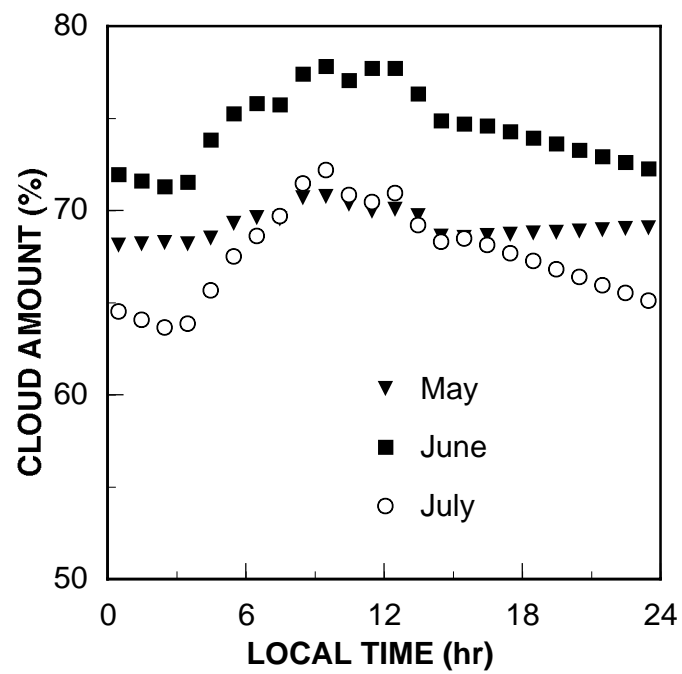


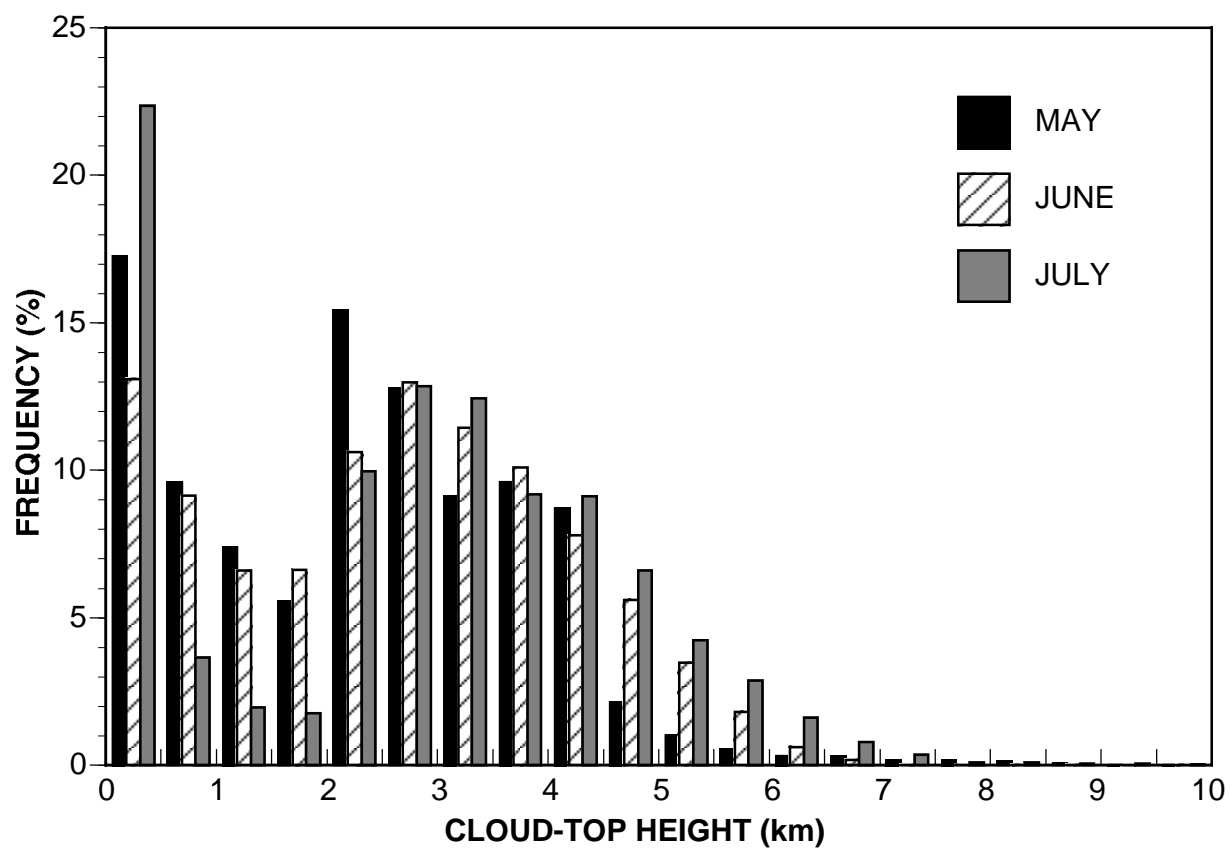


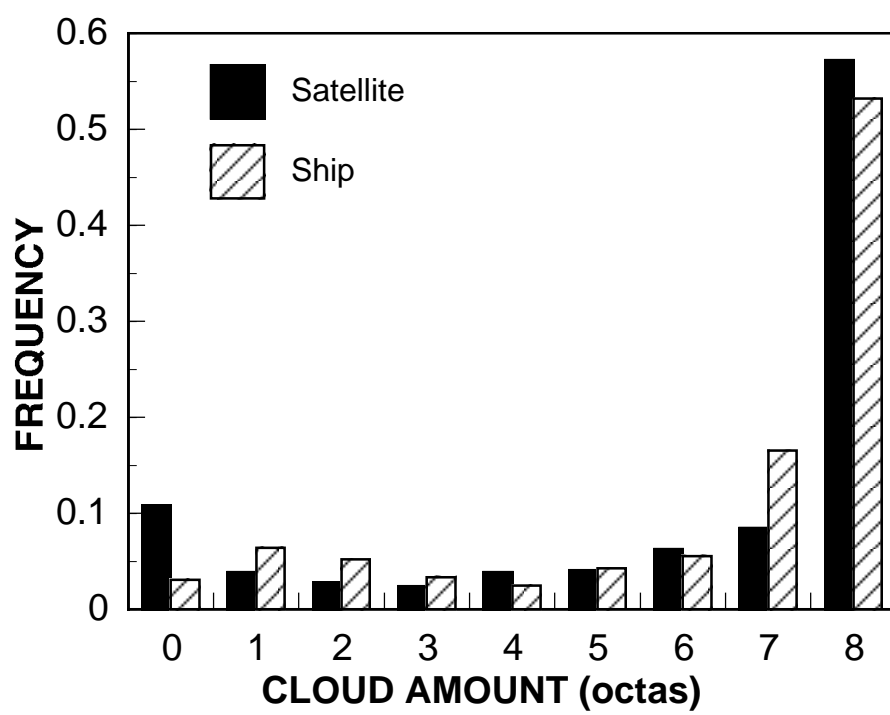


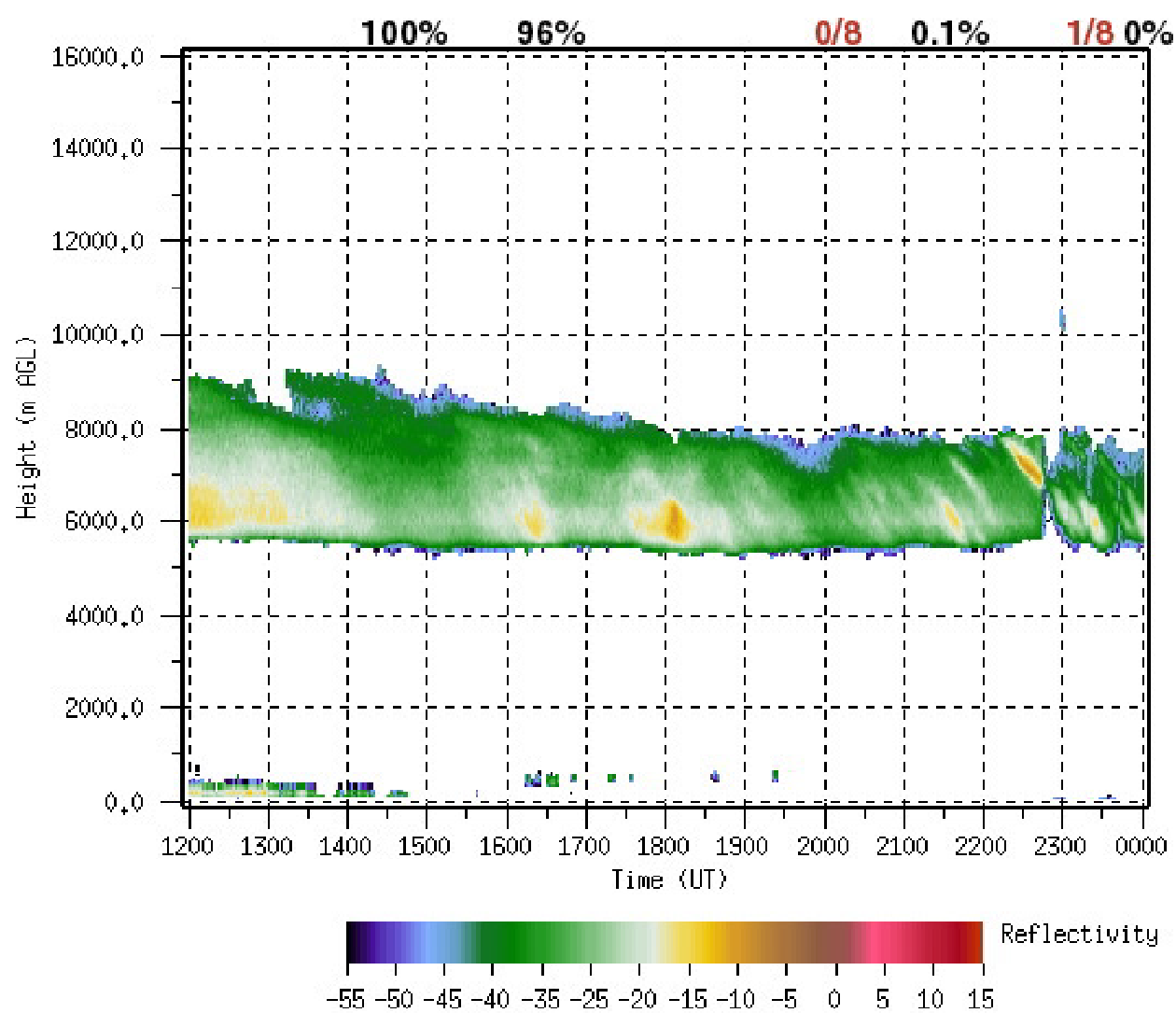


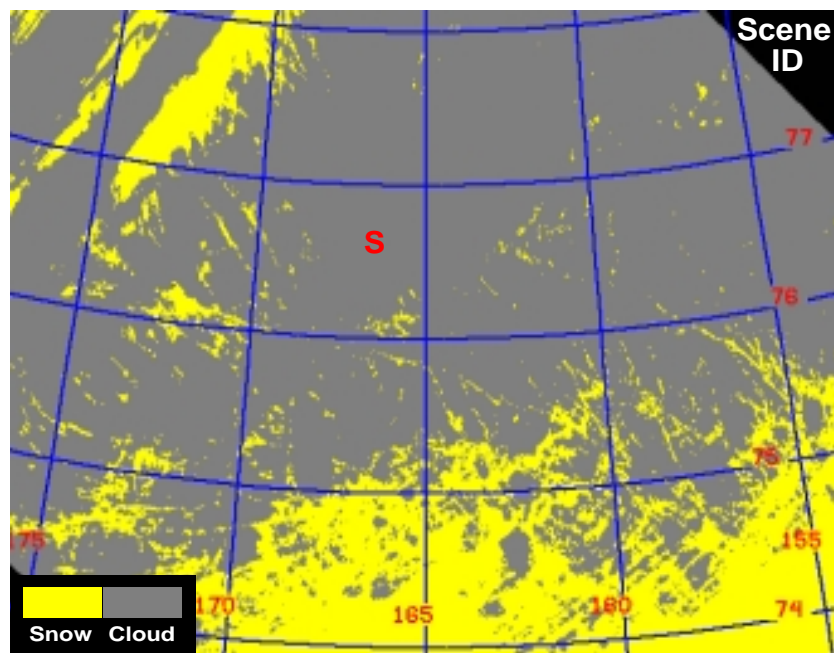
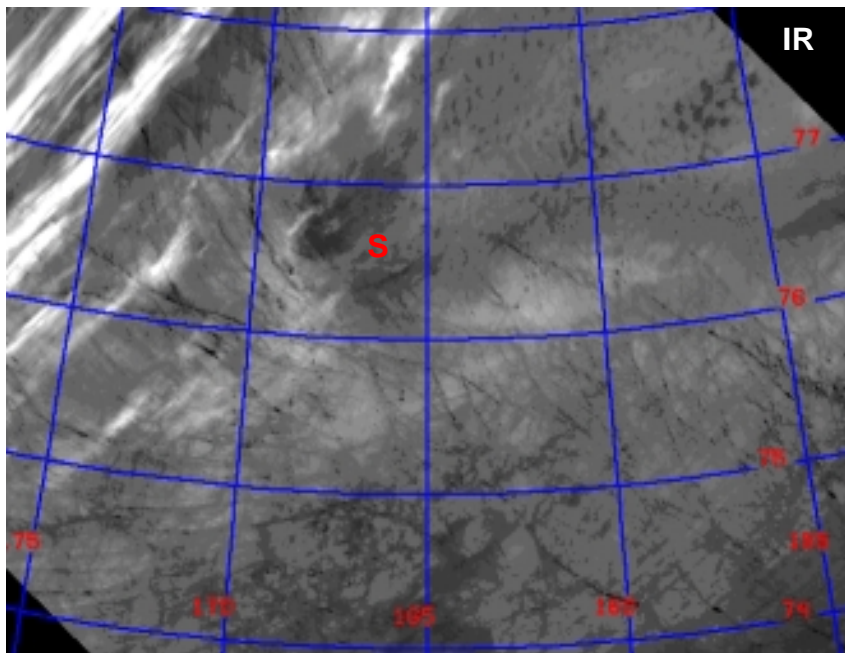
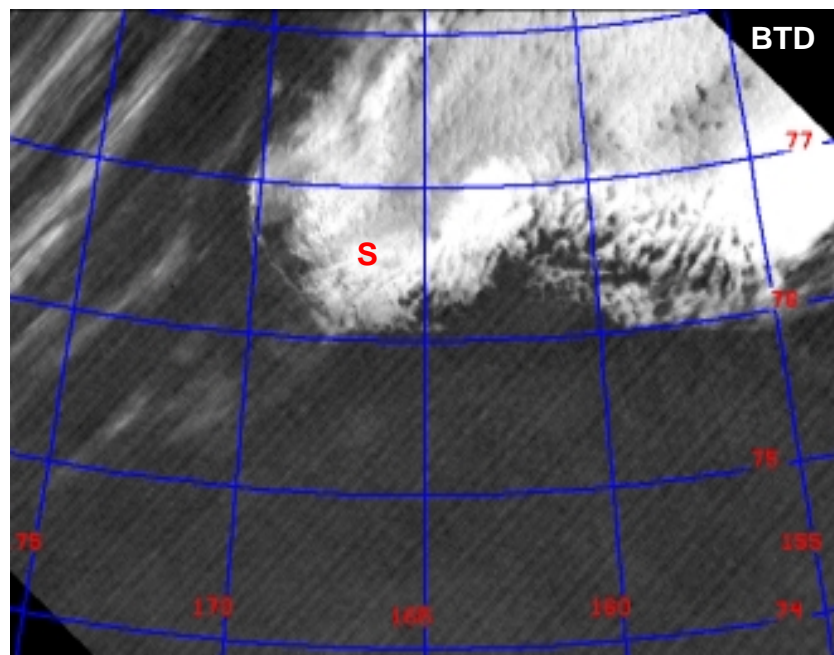
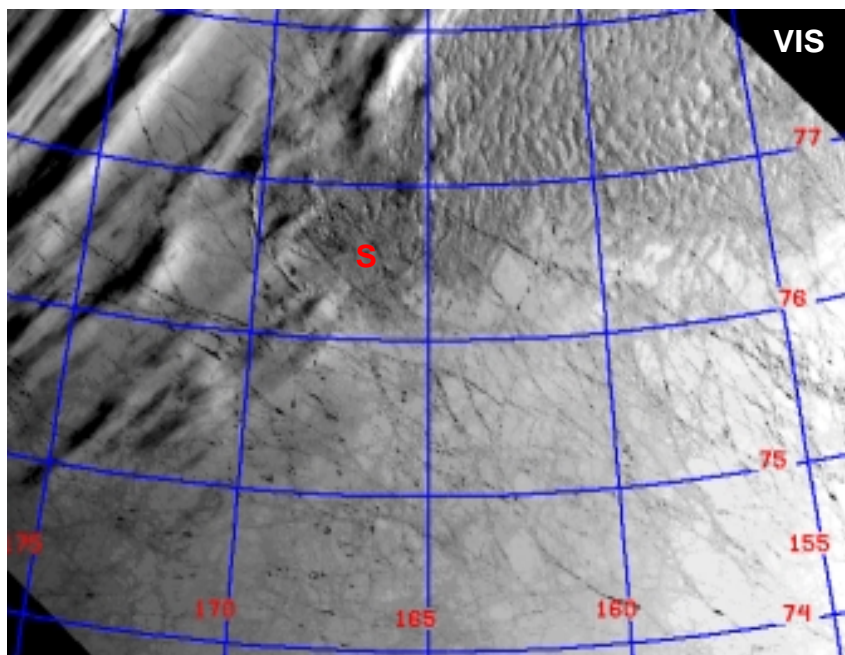


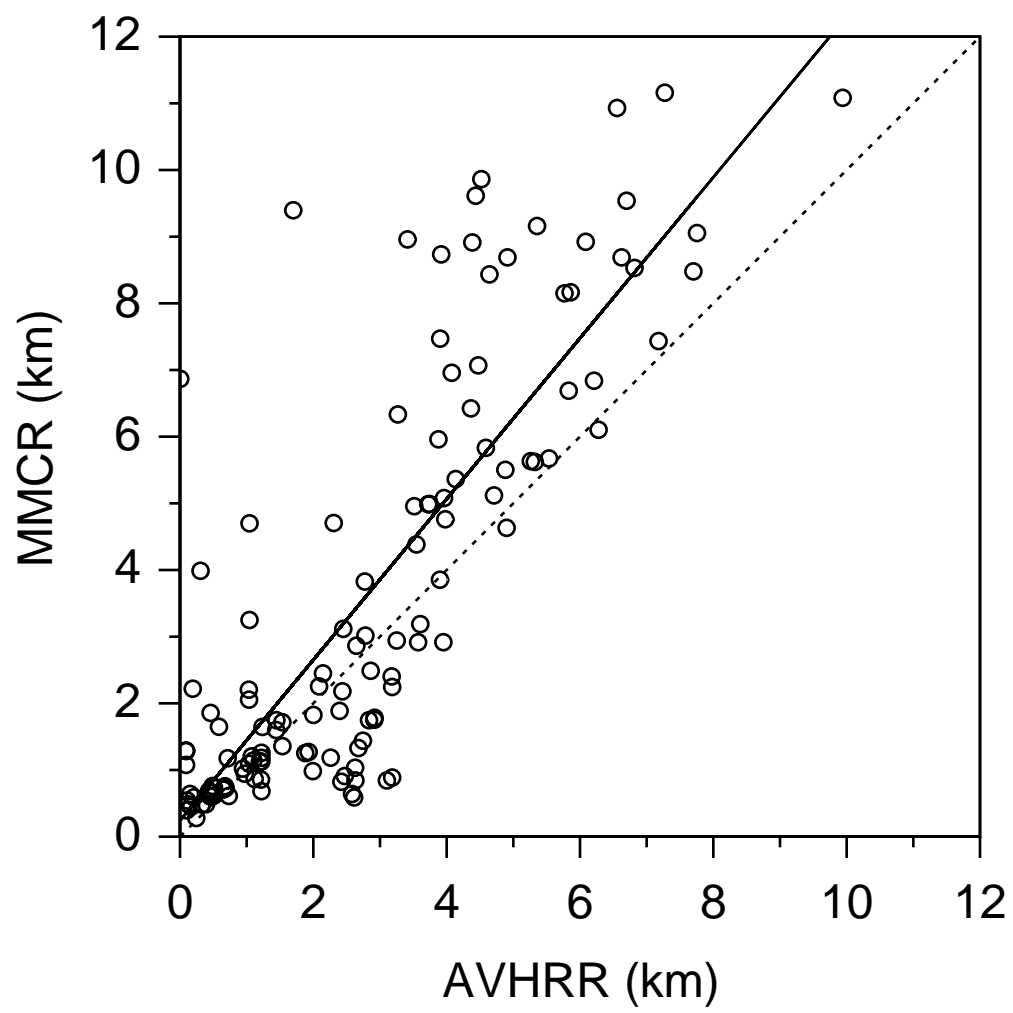


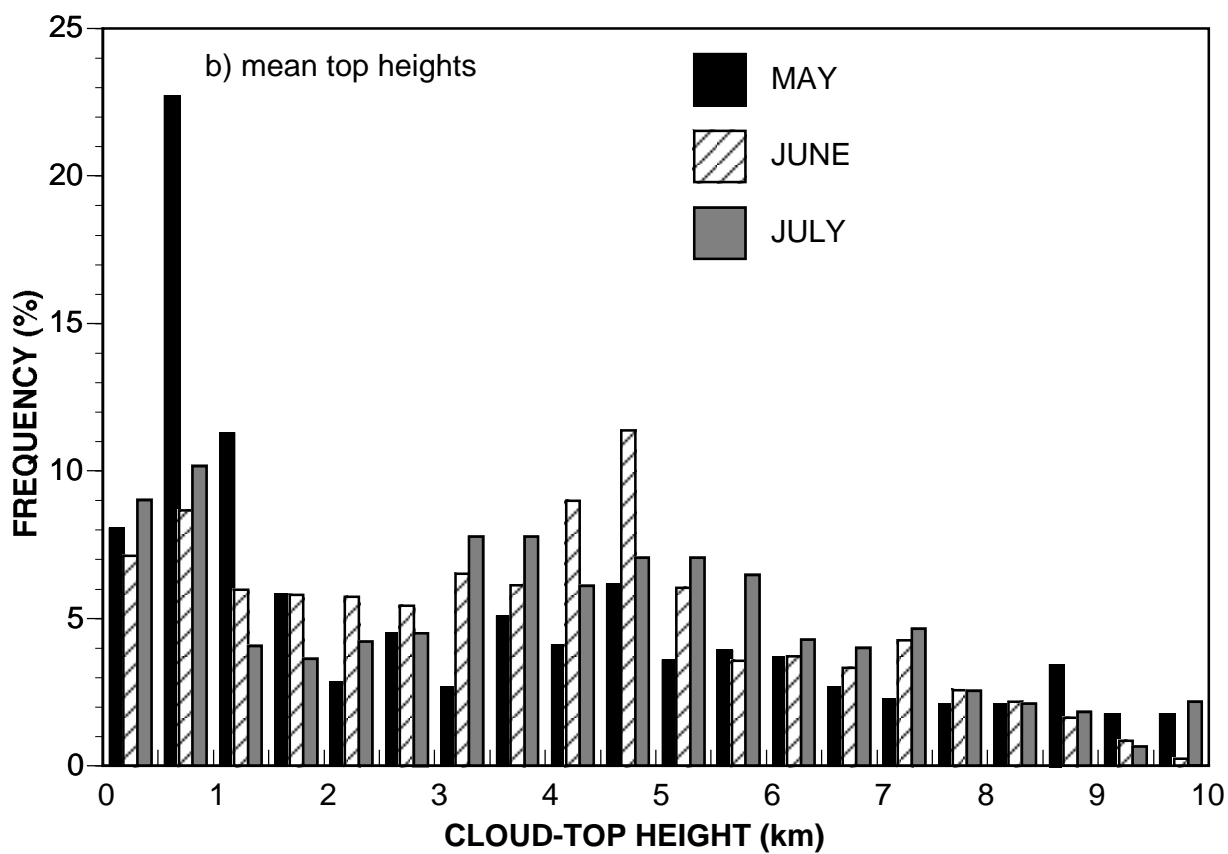
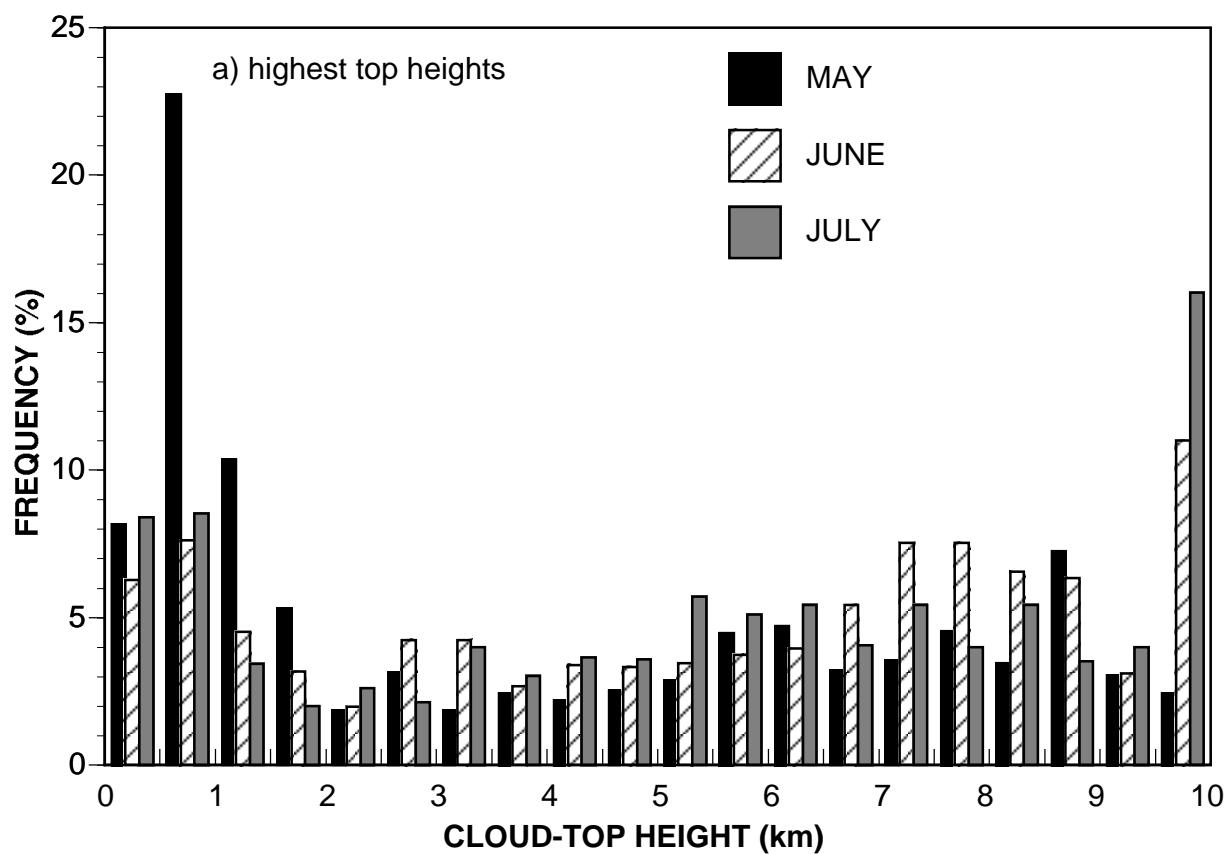




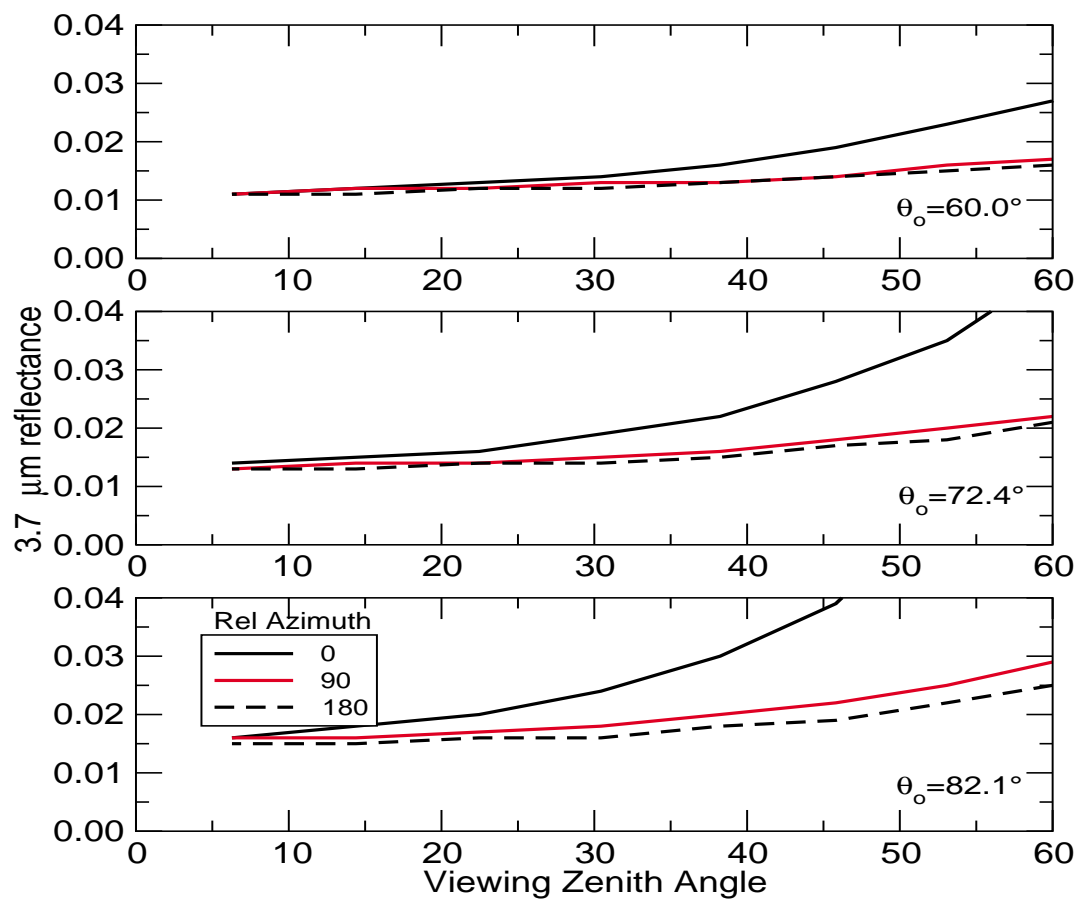








a)



b)

